

# A Redetermination of the Hubble Constant with the Hubble Space Telescope from a Differential Distance Ladder<sup>1</sup>

Adam G. Riess<sup>2,3</sup>, Lucas Macri<sup>4</sup>, Stefano Casertano<sup>3</sup>, Megan Sosey<sup>3</sup>, Hubert Lampeitl<sup>3,9</sup>, Henry C. Ferguson<sup>3</sup>, Alexei V. Filippenko<sup>5</sup>, Saurabh W. Jha<sup>6</sup>, Weidong Li<sup>5</sup>, Ryan Chornock<sup>5</sup>, and Devdeep Sarkar<sup>8</sup>

## ABSTRACT

This is the second of two papers reporting results from a program to determine the Hubble constant to  $\sim 5\%$  precision from a refurbished distance ladder based on extensive use of differential measurements. Here we report observations of 240 Cepheid variables obtained with the Near Infrared Camera and Multi-Object Spectrometer (NICMOS) Camera 2 through the  $F160W$  filter on the *Hubble Space Telescope* (*HST*). The Cepheids are distributed across six recent hosts of Type Ia supernovae (SNe Ia) and the “maser galaxy” NGC 4258, allowing us to *directly* calibrate the peak luminosities of the SNe Ia from the precise, geometric distance measurements provided by the masers. New features of our measurement include the use of the same instrument for all Cepheid measurements across the distance ladder and homogeneity of the Cepheid periods and metallicities thus necessitating only a *differential* measurement of Cepheid fluxes and reducing the largest systematic uncertainties in the determination of the fiducial SN Ia luminosity. In addition, the NICMOS measurements reduce the effects of differential extinction in the host galaxies by a factor of  $\sim 5$  over past optical data. Combined with a greatly expanded set of 240 SNe Ia at  $z < 0.1$  which define their magnitude-redshift relation, we find  $H_0 = 74.2 \pm 3.6 \text{ km s}^{-1} \text{ Mpc}^{-1}$ , a 4.7% uncertainty including both statistical and systematic errors. To independently test the maser calibration, we use the ten individual parallax measurements of Galactic Cepheids obtained with the *HST* Fine Guidance Sensor and find similar results. We show that the factor of 2.2 improvement

---

<sup>1</sup>Based on observations with the NASA/ESA *Hubble Space Telescope*, obtained at the Space Telescope Science Institute, which is operated by AURA, Inc., under NASA contract NAS 5-26555.

<sup>2</sup>Department of Physics and Astronomy, Johns Hopkins University, Baltimore, MD 21218.

<sup>3</sup>Space Telescope Science Institute, 3700 San Martin Drive, Baltimore, MD 21218; ariess@stsci.edu .

<sup>4</sup>Department of Physics, Texas A&M University, 4242 TAMU, College Station, TX 77843-4242.

<sup>5</sup>Department of Astronomy, University of California, Berkeley, CA 94720-3411.

<sup>6</sup>Department of Physics and Astronomy, Rutgers University, 136 Frelinghuysen Road, Piscataway, NJ 08854.

<sup>7</sup>Smithsonian Astrophysical Observatory, Cambridge, MA

<sup>8</sup>UC Irvine

<sup>9</sup> Institute of Cosmology and Gravitation, University of Portsmouth, Portsmouth, PO1 3FX, UK

in the precision of  $H_0$  is a significant aid to the determination of the equation-of-state parameter of dark energy,  $w = P/(\rho c^2)$ . Combined with the Wilkinson Microwave Anisotropy Probe 5-year measurement of  $\Omega_M h^2$ , we find  $w = -1.12 \pm 0.12$  independent of any information from high-redshift SNe Ia or baryon acoustic oscillations (BAO). This result is also consistent with analyses based on the combination of high-redshift SNe Ia and BAO. The constraints on  $w(z)$  now including high-redshift SNe Ia and BAO are consistent with a cosmological constant and are improved by a factor of 3 due to the refinement in  $H_0$  alone. We show that future improvements in the measurement of  $H_0$  are likely and should further contribute to multi-technique studies of dark energy.

*Subject headings:* galaxies: distances and redshifts — cosmology: observations — cosmology: distance scale — supernovae: general

## 1. Introduction

The *Hubble Space Telescope (HST)* established a cornerstone in the foundations of cosmology by observing Cepheid variables beyond the Local Group, leading to a measurement of the Hubble constant ( $H_0$ ) with 10%–15% precision (Freedman et al. 2001; Sandage et al. 2006). This measurement resolved decades of extreme uncertainty about the scale and age of the Universe. The discovery of cosmic acceleration and the dark energy that drives it (Riess et al. 1998; Perlmutter et al. 1999; see Friemann, Huterer, & Turner 2008 and Filippenko 2005 for reviews) has intensified the need for ever-higher-precision measurements of  $H_0$  to constrain and test the new cosmological models. Observations are essential to determine, empirically, aspects of the new model including its geometry, age, mass density, and the dark energy equation-of-state parameter,  $w = P/(\rho c^2)$ , where  $P$  is its pressure and  $\rho$  its energy density. Perhaps the most fundamental question is whether dark energy is a static, cosmological constant or a dynamical, inflation-like scalar field — or whether it can be accommodated at all within the framework of General Relativity.

While measurements of the high-redshift Universe from the cosmic microwave background (CMB), baryon acoustic oscillations (BAO), and Type Ia supernovae (SNe Ia) in concert with a fully parameterized cosmological model can be used to *predict* the Hubble constant (e.g., Spergel et al. 2007; Komatsu et al. 2008), they are not a substitute for its *measurement* in the local Universe. Using all of these measures and the *assumptions* that  $w = -1$  and that space is flat, a predicted precision of 2% in the Hubble constant may be inferred (see Table 1 for  $\Lambda$ CDM) (Komatsu et al. 2008). However, significant tension (at the  $3\sigma$  level) exists in the value of  $H_0$  predicted from CMB+BAO and CMB+high- $z$  SNe Ia when the other cosmological parameters such as curvature and  $w$  are constrained only by data (see Table 1;  $\text{OWCDM}$ ). This suggests that something interesting about the model or the measurements would be learned from an independent determination of  $H_0$  of comparable precision.

Increasing the precision of the measurement of the Hubble constant requires reducing system-

Table 1:  $H_0$  Inferred from 5-year WMAP Combined with the Most Constraining Data

Data set	$\Lambda$ CDM ( <i>i.e.</i> , $\Omega_K \equiv 0, w \equiv -1$ )	OWCDM ( <i>i.e.</i> , $\Omega_K = \text{free}, w = \text{free}$ )
WMAP5	$71.9^{+2.6}_{-2.7}$	$47^{+14}_{-12}$
WMAP5 + BAO	$70.9 \pm 1.5$	$81.7^{+6.5}_{-6.4}$
WMAP5 + high- $z$ SNe	$69.6 \pm 1.7$	$57.5 \pm 4.8$
WMAP5 + BAO + high- $z$ SNe	$70.1 \pm 1.3$	$68.7^{+1.9}_{-2.0}$

Note: The constraints on  $H_0$  are based on the WMAP team’s analysis of the 5-year WMAP data combined with other data sets (Komatsu et al. 2008), as listed; see <http://lambda.gsfc.nasa.gov/product/map/dr3/parameters.cfm> High- $z$  SNe refers to measurements of the magnitude– $z$  relation of SNe without reference to their distance scale.

atic uncertainties which dominate the error budget along the conventional distance ladder (Freedman et al. 2001; Leonard et al. 2003). As the Hubble diagram of SNe Ia establishes the *relative* expansion rate to an unprecedented uncertainty of  $<1\%$  (e.g., Hicken et al. 2009) the calibration of the luminosity of SNe Ia affords the greatest potential for precision in measuring  $H_0$ . As we show in §4, the largest sources of systematic error along this route come from the use of uncertain transformations to meld heterogeneous samples of Cepheids observed with different photometric systems in the anchor galaxy and SN Ia hosts.

### 1.1. The SHOES Program

The goal of the SHOES Program (Supernovae and  $H_0$  for the Equation of State) (*HST* Cycle 15, GO-10802) is to measure  $H_0$  to  $<5\%$  precision by mitigating the dominant systematic errors.<sup>1</sup> To obviate the limited accuracy of photographic SN data, we have been calibrating recent SNe Ia recorded with modern detectors and acquiring uniform samples of Cepheids observed in the SN Ia hosts and in the anchor galaxy. Progress in the former was presented by Riess et al. (2005, 2009), more than doubling the sample of high-quality calibrators by providing reliable calibration for four modern SNe Ia. Here we address the latter, reporting the results of infrared (IR) observations of Cepheids which are homogeneous in their periods, metallicities, and measurements in both the anchor (NGC 4258) and the SN hosts.

NGC 4258 offers attractive benefits over the use of the Large Magellanic Cloud (LMC) or the Milky Way Galaxy as an anchor of the distance ladder: (1) all of its Cepheids can be treated as being at a *single distance* determined *geometrically* from the Keplerian motion of its masers as  $7.2 \pm 0.5$  Mpc (Herrnstein et al. 1999); (2) more than a decade of tracking its masers has resulted in

---

<sup>1</sup>The *HST* observations were also designed to find SNe Ia at  $z > 1$  with coordinated ACS parallel observations. Two high- $z$  SNe were found before the failure of ACS on 2007 Feb. 1.

little change to its distance while steadily increasing its *precision* from 7% (Herrnstein et al. 1999) to 5.5% (Humphreys et al. 2005), to 3% (Humphreys et al. 2008, 2009, Greenhill et al. 2009) (3) the geometric distance measurement can be internally cross-checked via proper motion and centripetal acceleration and the method can be externally tested by measurements of other maser systems (Braatz et al. 2008, Greenhill et al. 2009); (4) its Cepheids have a metallicity similar to those found in the hosts of SNe Ia (Riess et al. 2009); (5) *HST* observations of NGC 4258 from Cycles 12, 13, and 15 provide the largest sample of long-period ( $P > 10$  d) Cepheids (Macri et al. 2006, 2009); and (6) its Cepheids can be observed with *HST* in exactly the same manner as those in SN Ia hosts. In §4, we independently test the use of the distance to NGC 4258 by adopting the individual parallax measurements of Galactic Cepheids from Benedict et al. (2007).

The IR observations of Cepheids presented in §3 provide additional advantages over those in the optical: (1) reducing the differential extinction by a factor of five over visual data, and (2) reducing the dependence of Cepheid magnitudes on chemical composition (Marconi et al. 2005). The resulting, refurbished distance ladder builds on past work while removing four of the largest systematic sources of uncertainty in  $H_0$ . In §3 and §4 we show that the total uncertainty in the measurement of  $H_0$  has been reduced from 11% (Freedman et al. 2001) to 4.8%.

## 2. NICMOS Cepheid Observations of the SHOES Program

In Riess et al. (2009), we used *HST*/ACS+WFPC2 observations to discover Cepheids in two new SN Ia hosts and to expand previous samples in four other SN Ia hosts with newly discovered, longer-period ( $P > 60$  d) variables. In Macri et al. (2009) we used *HST*/ACS+WFPC2 observations to augment the Cepheid sample in NGC 4258. These new observations, together with those from Saha et al. (1996, 1997, 2001), Gibson et al. (2000), Stetson & Gibson (2001), and Macri et al. (2006) provide the position, period, and phase of 450 Cepheids in 6 hosts with reliable SN Ia data and NGC 4258 with typically 14 epochs of *HST* imaging with *F555W* and 1–5 epochs with *F814W* (except for NGC 4258, which has 12 epochs of *F814W* data).

The Near Infrared Camera and Multi-Object Spectrometer (NICMOS) on *HST* provides the means to obtain near-IR measurements of optically identified Cepheids. Macri et al. (2001) used short exposures ( $\sim 1$  ksec) with NICMOS to measure 70 extragalactic Cepheids in 14 galaxies at an average distance of 5 Mpc (including 2 Cepheids in NGC 4536) to verify the Galactic extinction law.

In *HST* Cycle 15 the SHOES program obtained deep (10 to 35 ksec), near-IR observations of the Cepheids in these SN Ia hosts. The SN Ia in each host was chosen for meeting the following criteria: (1) has modern data (i.e., photoelectric or CCD), (2) was observed before maximum brightness, (3) has low reddening, (4) is spectroscopically typical, and (5) has optical *HST*-based observations of Cepheids in its host. The resulting sample consists of 6 SN Ia hosts given in Table 2. The six members and their SNe are shown in Figure 1. In Cycle 15 we also obtained 2 ksec

NICMOS imaging of Cepheids in NGC 4258 to augment that obtained in Cycle 13 by GO 10399 (P.I. Greenhill).

Table 2: Cepheid Hosts Observed by SHOES

Host	SN Ia	Initial optical	HST Cycle	Reobservation, Cycle 15	Observation near-IR, Cycle 15
NGC 4536	SN 1981B	WFPC2	4	WFPC2	NIC2
NGC 4639	SN 1990N	WFPC2	5	ACS	NIC2
NGC 3982	SN 1998aq	WFPC2	8	ACS	NIC2
NGC 3370	SN 1994ae	ACS	11	ACS	NIC2
NGC 3021	SN 1995al	ACS	14	ACS	NIC2
NGC 1309	SN 2002fk	ACS	14	ACS	NIC2
NGC 4258	————	ACS	12	ACS/WFPC2	NIC2 <sup>a</sup>

<sup>a</sup>Some NIC2 data obtained in Cycle 13

### 2.1. NICMOS Data Reduction

Groupings of optically-characterized Cepheids were observed using the NICMOS Camera 2 and the *F160W* filter. This camera offers the best compromise of area and sampling of the point-spread function (PSF) of the three NICMOS cameras. For each SN host galaxy we selected four to five 0.1 sq arcmin pointings of 3–12 orbit depth (10–35 ks) to contain multiple previously identified long-period Cepheids. The pointing centers and total integration times are given in Table 3. The imaging configurations are shown in Figures 2 to 7. The observations were obtained in single-orbit visits spread over  $\sim 2$  months.

We developed an automated pipeline to calibrate the raw NICMOS frames. The first step subtracted one of two “superdarks” produced from archival data obtained after the installation of the NICMOS Cooling System, corresponding to the closest temperature state (of two primary temperature regimes) at which the data were obtained. Next, the data were processed through the STScI-supported CALNICA pipeline with the following additions. The STSDAS routine BIASEQ (Bushouse et al. 2000) was used after the corrections for bias, dark counts, and linearity to account for stochastic changes in quadrant bias level. After flat-fielding, cosmic-ray rejection, and count-rate conversion, the images were corrected for the count-rate nonlinearity as calibrated by de Jong et al. (2006). The remaining quadrant-dependent linear DC bias was fit and removed using the PEDSUB task. Any data obtained soon after a passage by *HST* through the South Atlantic Anomaly (SAA) were corrected for the persistence of cosmic rays using a post-SAA dark frame and the routine SAACLEAN (Bergeron & Dickinson 2003).

Approximately 10% of our images were contaminated by charge persistence after the detector was exposed to the bright limb of the Earth in the preceding orbit. The structure of the persistence image is time independent and is a map of the density of charge traps saturated by the Earth light.

A persistence image was produced from the data which was then scaled and subtracted from the affected data as described by Riess & Bergeron (2008).

Residual amplifier glow and its persistence were removed by subtracting a model of the sky image from the combination of all exposures in a visit. The model was smoothed with a ring filter (larger in diameter than the PSF) to ensure that stellar sources in the data were not present in this sky model.

Next we combined the exposures from each visit to produce a full image combination for each pointing listed in Table 3. We first registered the exposures within a visit using the dither positions indicated in the image headers. To register images between visits we used between 30 and 100 bright sources to empirically measure the shifts and rotations between visits (we also verified that scale variations between orbits were negligible). The typical root-mean square (rms) deviation of sources between our visit-to-visit registration solutions was 0.2-0.3 pixels, yielding an error in the mean of less than 0.05 pixels. The final image combination was resampled on a pixel scale of  $0.038''$  using the drizzle algorithm (Fruchter & Hook 2002).

Because the PSF of NIC2 with  $F160W$  is well sampled, our image combination should cause little broadening of the PSF. To test this, we measured the difference in the photometry of non-variable supergiants in single epochs and in the full image combinations. The median difference was  $\sim 0.003$  mag (in the sense of the combination being brighter, opposite the expected direction if the effect were real) and consistent with zero to within the statistical uncertainty. Thus we concluded there was no loss in accuracy of the photometry obtained by combining images from individual visits.

To identify the precise positions of Cepheids in the NICMOS image combinations, we derived the geometric transformation from the  $HST$   $F814W$  images to the  $F160W$  images, iteratively matching bright to faint sources to find sources in common. This registration empirically determined the difference in plate scale between ACS, WFPC2, and NIC2. Typically we identified more than 100 sources in common, resulting in an uncertainty in the mean Cepheid position of  $<0.03$  pixels (1 milliarcsec).

## 2.2. NICMOS Cepheid Photometry

We developed software to measure Cepheid photometry in crowded NICMOS images based on the procedures established for  $HST$  optical photometry (Stetson 1994; Saha et al. 1996). Since we know *a priori* the precise position of the Cepheids in our NICMOS data, we can fix the positions in the NICMOS images to mitigate the measurement bias which can arise naturally for flux measurements of sources made from the same data used for their discovery (Hogg & Turner 1998).

We derived a model of the PSF in our NICMOS images using observations of the bright solar analogue, P330E, averaged over several visits and processed in the same way our host images. P330E

provides a fundamental standard for the NICMOS Vega magnitude zeropoint ( $F160W = 11.45$  mag, Vega system) and our natural system magnitudes are measured relative to this zeropoint. However, the difference between the photometry of Cepheids in NGC 4258 and the SN hosts, employed to measure  $H_0$  in §3, are *independent* of the adopted zeropoint.

For each known Cepheid, we produced a list of neighboring stars in the NICMOS images within its “critical” radius ( $4 \times \text{FWHM}$ , where FWHM is the full width at half-maximum intensity) or within that of one of its neighbors. Together, these stars and the Cepheid define a “crowded group” whose members must be modeled together. Initially, we subtracted a PSF model at the location of the Cepheid (as determined from the optical data) and then used the algorithm *DAOFIND* to identify neighboring stars within the critical radius but at least  $0.75 \times \text{FWHM}$  beyond each Cepheid. Stellar sources within and beyond the group were modeled and subtracted, and the background level for the group was determined from the mode of the pixels in an annulus around the Cepheid with an inner radius of 15 pixels and an outer radius of 20 pixels.

We then used a Levenberg-Maquardt-based algorithm to find the most likely values and uncertainties of the group parameters by minimizing the  $\chi^2$  statistic between the image and model pixels within the critical radii of the modeled sources. For all non-Cepheid sources, their positions were allowed to vary within 0.5 pixels of their original detected position and the amplitudes were allowed to vary. For the Cepheids, only the amplitude of the PSF was varied. The Cepheid position determined from the optical images was fixed, as was the group sky level. Our typical group had 5 to 15 unresolved, modeled sources besides the Cepheids producing 3 times this number of free parameters plus one additional parameter for the Cepheid brightness. The individual pixel noise was relatively uniform, resulting from a combination of sky, dark current and read noise.

After identifying the optimal solution, we subtracted the model from the data and inspected the residuals to determine the best set of global photometry parameters for all images. In Figure 8 we show as an example the image, model, and residuals of the groups for one of the richest NICMOS pointings, NGC3370-GREEN, with 14 Cepheids over a wide range of periods.

### 2.3. Sky Determination and Bias Correction

The surroundings of the Cepheids are mottled, with unresolved sources and surface brightness fluctuations whose fluxes are generally fainter but occasionally brighter than our target Cepheids (see Fig. 10, NGC 4258 and NGC 3370 GREEN field). These scenes pose a challenge to estimating the correct background level for the Cepheids. Simply measuring the mean flux in an annulus centered on the Cepheid would provide an unbiased but very noisy estimate of the background.

Instead, we follow the conventional approach of determining the sky level from the sky annulus after first subtracting models of the stellar sources within it. Because we would expect a similar number of background sources coincident with (yet inseparable from) the Cepheid, we would naturally *underestimate* the sky level for the Cepheid. Though this bias is ameliorated somewhat by

the use of the mode statistic from the residual image as discussed by Stetson (1987), a bias still remains.

In previous work it has been shown that this photometric bias in optically-selected Cepheid samples is reduced by the act of selecting Cepheids with strong amplitudes and statistically significant variations in flux (Ferrarese et al. 2000). The addition of significant, blended flux would reduce the amplitude of the Cepheid, increase the model uncertainty and reduce the significance of true variations. However, this mechanism does not apply to the NICMOS images as they were not used to select Cepheids. Indeed, Cepheids are bluer than a common source of blending, red giants, so the blending bias in the NICMOS data can be significant. Macri et al. (2001) found this photometric bias to vary from negligible to 0.1 mag for the Cepheids discovered with WFPC2 and reobserved with NICMOS, and measured the impact to artificial stars injected in the vicinity of each Cepheid to correct for this effect. We adopt the same approach here.

In addition, we can improve our estimate of the blending bias. On average, the displacement of a Cepheid’s centroid in the NICMOS data relative to its optically determined position correlates with the degree of blending in the NICMOS data. For randomly located sources of blending, brighter blended sources cause larger Cepheid displacements and bias. For artificial stars rediscovered within  $\sim 0.1$  pixels of their injected position we find  $< 0.1$  mag of blending bias. The photometric bias grows linearly with the displacement of the centroid, rising to  $\sim 0.3$  mag for a full pixel ( $0.038''$ ) displacement. Beyond a pixel, the recovered star is often not the same as the one injected (as occurs when the injected star is too faint to be found), and any relation between the displacement and bias dissipates. Rarely, a Cepheid will be *exactly* coincident with a bright source causing it to be an outlier in the  $P$ - $L$  relation. Such complete blends are later eliminated from both our sample (and the artificial star simulations) with a  $2.5\sigma$  rejection from the mean, a threshold based on Chauvenet’s criterion (i.e., less than half a Cepheid would be expected to exceed the outlier limit for a Gaussian distribution of residuals).

To determine the individual photometric correction for each Cepheid we added 1000 artificial stars at random positions within a radius of  $0.05''$  to  $0.75''$  from each Cepheid. The magnitudes of the artificial stars were given by the Cepheid magnitude *predicted* by its period using an initial fit (i.e., uncorrected) to the period-magnitude relations. After correcting the Cepheid magnitudes for the measured bias, these relations were refit and the process was repeated until convergence. The dispersion of the artificial stars was used to estimate the uncertainty in the magnitude of the Cepheid by adding this term in quadrature to the Cepheid measurement uncertainty. An example of this artificial-star analysis is shown in Figure 9 for a  $P = 59$  d Cepheid in our second-most-distant galaxy, NGC 3021.

For NGC 4258, our anchor galaxy, the median bias correction was 0.14 mag ( $\pm 0.014$ ) and for the SN hosts the median was 0.16 ( $\pm 0.021$ ) mag. Thus we conclude that *the photometric corrections for the Cepheids in NGC 4258 and the SN hosts are extremely similar*. This is not surprising as the apparent stellar density of the fields is also quite similar as seen in Figure 10. Although NGC

4258 is closer than the SN hosts, reducing its relative crowding, the NGC 4258 inner fields (Macri et al. 2006) are closer to the nucleus where the true stellar density is greater.

Because the luminosity calibration of SNe Ia depends on only *the difference* in the magnitudes of the Cepheids in the anchor galaxy and the SN hosts, the net effect of blending even without correction is quite small:  $\sim 0.02$  mag, or about 1% in the distance scale. However, our corrections account for this small difference as further addressed in §4.2.

Artificial-star simulations cannot account for blending which is local to the Cepheids (i.e., binarity or cluster companions). However, we expect little net effect from such blending (after the removal of outliers) as such blending is likely to occur with similar frequency in the anchor and SN hosts and thus would largely cancel in their difference.

Because the amplitudes of IR light curves are  $< 0.3$  mag, even magnitudes measured at random phases provide comparable precision to the mean flux for determining the period-luminosity ( $P-L$ ) relation (Madore & Freedman 1991). As our exposures were obtained over  $\sim 2$  months the magnitude measured from the mean image will have a dispersion of  $< 0.08$  mag around the mean flux. To account for this error, we correct the measured magnitude to the mean-phase magnitude using the Cepheid phase, period, and amplitude from the optical data, the dates of the NICMOS observations, and the Fourier components of Soszynski et al. (2005) which quantify the relations between Cepheid light curves in the optical and near-IR. These phase corrections were found to be insignificant in the subsequent analysis.

Table 4 contains the aforementioned parameters for each Cepheid. The Cepheid’s NIC2 field, position, identification number (from Riess et al. 2009 and Macri et al. 2006), period, mean  $V - I$  color,  $F160W$  mag and its uncertainty are given in the first 8 columns. Column 9 contains the displacement of the Cepheid in the NICMOS data from optical position in pixels of  $0.038''$  size. Column 10 gives the photometric bias determined from the artificial star tests for the Cepheid’s environment and displacement and are already added to determine column 7. Column 11 contains the correction from the sampled phase to the mean and has already been subtracted to determine column 7. Column 12 contains the metallicity parameter,  $12 + \log[\text{O}/\text{H}]$ , inferred at the position of each Cepheid. Column 13 and 14 contains the rejection flag employed and the source of the Cepheid detection as noted in Table 4, respectively.

Table 3: NIC2 *F160W* Cepheid Observations

Target	$\alpha$ (J2000)	$\delta$ (J2000)	Exp time (s)
NGC1309-BLUE	3 <sup>h</sup> 22 <sup>m</sup> 3.499 <sup>s</sup>	−15° 24′ 4.242″	10,239.5
NGC1309-YELLOW	3 22 7.040	−15 24 26.800	23,031.0
NGC1309-CYAN2	3 22 8.790	−15 24 46.148	34,174.3
NGC1309-GREEN	3 22 9.862	−15 23 48.548	10,239.5
NGC3021-BLUE	9 50 55.493	33 32 48.598	10,239.5
NGC3021-CYAN	9 50 54.079	33 33 28.190	10,239.5
NGC3021-GREEN	9 50 59.984	33 33 5.202	20,478.9
NGC3021-RED	9 50 57.330	33 33 36.883	20,158.9
NGC3370-BLUE	10 47 4.334	17 17 3.726	20,478.9
NGC3370-CYAN	10 47 6.432	17 15 26.429	10,239.5
NGC3370-GREEN	10 47 1.673	17 16 56.221	26,238.7
NGC3370-RED	10 47 8.354	17 15 48.264	10,239.5
NGC3982-BLUE	11 56 24.458	55 7 13.644	17,919.0
NGC3982-CYAN-COPY	11 56 32.368	55 7 30.329	7,679.6
NGC3982-GREEN	11 56 21.375	55 7 23.696	7,679.6
NGC3982-RED-COPY	11 56 23.150	55 6 38.776	17,919.0
NGC3982-YELLOW	11 56 30.253	55 7 54.595	10,239.5
NGC4536-BLUE	12 34 18.360	2 11 35.570	17,919.0
NGC4536-CYAN	12 34 21.395	2 13 10.230	12,799.3
NGC4536-GREEN	12 34 17.313	2 13 6.429	17,919.0
NGC4536-RED	12 34 21.371	2 12 6.289	17,919.0
NGC4639-BLUE	12 42 53.114	13 14 54.342	10,239.5
NGC4639-BLUE-LATE <sup>a</sup>	12 42 52.946	13 14 55.207	10,239.5
NGC4639-CYAN	12 42 49.300	13 16 9.272	19,966.9
NGC4639-GREEN	12 42 52.163	13 16 30.699	20,478.9
NGC4639-RED	12 42 56.438	13 15 20.369	10,239.5
NGC4258-NIC-POS4	12 18 50.76	47 19 24.2	2559.8
NGC4258-NIC-POS5	12 18 57.92	47 20 35.5	2559.8
NGC4258-NIC-POS3	12 18 47.52	47 20 05.1	2559.8
NGC4258-NIC-POS2	12 18 50.09	47 20 43.1	2559.8
NGC4258-NIC-POS1	12 18 50.77	47 21 09.3	2559.8
NGC4258-NIC-POS13	12 18 54.90	47 21 47.9	2559.8
NGC4258-NIC-POS11	12 19 20.28	47 14 54.0	2559.8
NGC4258-NIC-POS10	12 19 22.72	47 14 44.6	2559.8
NGC4258-NIC-POS9	12 19 08.93	47 12 25.2	2559.8
NGC4258-NIC-POS8	12 19 12.02	47 12 21.1	2559.8
NGC4258-NIC-POS12	12 19 25.32	47 13 44.2	2559.8
NGC4258-NIC-POS6	12 19 21.03	47 10 21.5	2559.8
NGC4258-NIC-POS7	12 19 25.39	47 09 41.2	2559.8
NGC4258-INNER-NIC-09	12 18 53.21	47 18 43.5	2559.8
NGC4258-INNER-NIC-10	12 18 54.50	47 19 00.9	2559.8
NGC4258-INNER-NIC-08	12 18 51.38	47 18 42.1	2559.8
NGC4258-INNER-NIC-12	12 18 54.72	47 19 16.5	2559.8
NGC4258-INNER-NIC-05	12 18 48.98	47 19 13.2	2559.8
NGC4258-INNER-NIC-13	12 18 55.88	47 20 17.8	2559.8
NGC4258-INNER-NIC-06	12 18 48.99	47 19 47.4	2559.8
NGC4258-INNER-NIC-04	12 18 48.21	47 20 10.1	2559.8
NGC4258-INNER-NIC-11	12 18 54.55	47 20 41.7	2559.8
NGC4258-INNER-NIC-01	12 18 45.28	47 20 02.2	2559.8
NGC4258-INNER-NIC-07	12 18 50.33	47 21 06.3	2559.8
NGC4258-INNER-NIC-02	12 18 47.64	47 20 58.2	2559.8
NGC4258-INNER-NIC-03	12 18 48.07	47 21 19.7	2559.8
NGC4258-OUTER-NIC-04	12 19 20.62	47 13 12.4	2559.8

Table 4. NICMOS Cepheids

Field	$\alpha$ (J2000)	$\delta$ (J2000)	Id	P (days)	$V - I$ (mag)	$F160W$ (mag)	$\sigma$ (mag)	Offset (pix)	Bias (mag)	Phase (mag)	[O/H]	Flag <sup>a</sup>	Src*
N4536-B	188.57747	2.193860	9491	19.79	1.10	24.20	0.24	0.52	0.06	0.06	8.69		psl
N4536-B	188.57760	2.192130	9935	42.81	1.05	23.59	0.19	0.35	0.04	-0.09	8.68		psl
N4536-B	188.57383	2.194050	12075	49.70	1.17	23.26	0.22	0.48	0.15	0.02	8.64		psl
N4536-C	188.58908	2.221220	3633	23.37	0.82	23.91	0.20	0.57	0.06	0.14	8.75		psl
N4536-G	188.57352	2.219870	6827	24.54	0.74	23.86	0.31	0.70	0.28	0.19	8.71		psl
N4536-G	188.57237	2.216330	5630	55.24	1.03	22.55	0.19	0.10	0.05	-0.09	8.72		psl
N4536-R	188.58741	2.202540	3571	20.98	0.78	24.02	0.39	0.95	0.29	0.07	8.89		psl
N4536-R	188.58842	2.204110	2692	31.59	1.09	23.71	0.20	0.57	0.20	-0.04	8.90		psl
N4536-R	188.59047	2.200050	6914	34.63	1.22	22.72	0.22	0.37	0.13	-0.03	8.92	rej	psl
N4536-R	188.59103	2.202740	4786	37.45	0.93	23.67	0.22	0.46	0.13	-0.03	8.93		psl
N4536-B	188.57908	2.191510	9023	19.90	0.51	24.40	0.30	0.72	0.22	0.04	8.69		lm
N4536-C	188.58946	2.220100	3607	80.17	0.69	22.79	0.25	0.34	0.03	0.01	8.76		lm
N4536-G	188.57149	2.218370	6582	38.84	1.43	23.57	0.20	0.24	0.05	0.00	8.70		lm
N4536-R	188.58811	2.199800	6233	25.30	0.64	23.31	0.23	0.65	0.25	0.09	8.89		lm
N4536-B	188.57932	2.199800	13	18.54	0.72	24.56	0.38	0.60	0.16	0.00	8.71		ps
N4536-R	188.58854	2.192987	5	30.25	1.14	23.64	0.22	0.52	0.15	0.00	8.89		ps
N4639-B	190.72103	13.24735	11893	26.59	1.09	25.83	0.47	1.15	0.29	0.06	8.98	rej	psl
N4639-B	190.72412	13.24921	8651	27.54	0.91	24.58	0.54	0.74	0.44	0.08	9.05		psl
N4639-B	190.71891	13.25026	16601	42.20	1.18	23.54	0.56	0.54	0.18	0.01	9.09		psl
N4639-B	190.72047	13.24661	12394	54.82	1.06	24.10	0.47	2.69	0.53	0.05	8.95		psl
N4639-B-L	190.72412	13.24921	8651	27.54	0.91	24.68	0.47	0.36	0.59	0.11	9.05		psl
N4639-B-L	190.71891	13.25026	16601	42.20	1.18	23.84	0.34	0.41	0.29	-0.02	9.09		psl
N4639-B-L	190.72047	13.24661	12394	54.82	1.06	23.80	0.33	8.76	0.06	-0.03	8.95		psl
N4639-C	190.70392	13.26827	40321	37.27	1.24	23.89	0.25	0.20	0.11	0.02	8.83		psl
N4639-C	190.70509	13.26793	39829	39.41	0.91	23.79	0.22	0.24	0.07	-0.07	8.86		psl
N4639-C	190.70451	13.26849	40158	52.16	1.09	24.26	0.27	0.32	0.16	-0.09	8.84		psl
N4639-C	190.70539	13.26932	61786	56.31	1.18	24.04	0.24	0.87	0.11	0.13	8.84		psl
N4639-G	190.71845	13.27400	30160	51.11	1.11	24.21	0.19	0.16	0.04	-0.00	8.69		psl
N4639-R	190.73302	13.25647	4481	34.24	0.97	24.08	0.19	0.08	0.16	0.00	8.88		psl
N4639-B	190.72165	13.25058	12430	39.53	0.93	25.23	0.67	2.33	0.70	0.01	9.11	rej	lm
N4639-B	190.72020	13.24847	13602	47.27	1.44	23.92	0.31	0.56	0.16	0.04	9.02		lm
N4639-B-L	190.72020	13.24847	13602	47.27	1.44	24.06	0.30	0.50	0.03	-0.02	9.02		lm
N4639-R	190.73314	13.25609	4383	42.43	1.09	23.98	0.22	0.38	0.09	-0.03	8.88		lm
N3370-B	161.76928	17.28204	24497	16.78	0.87	25.89	0.68	2.63	0.39	-0.05	8.86	low P	lm
N3370-B	161.76766	17.28206	21444	19.64	0.92	26.21	0.42	3.98	0.03	-0.06	8.91	low P	lm
N3370-B	161.76554	17.28584	15081	32.56	1.22	25.56	0.39	0.98	0.34	0.00	8.80		lm
N3370-B	161.76923	17.28640	21445	37.10	1.07	24.67	0.20	0.47	0.14	-0.14	8.68		lm
N3370-B	161.76844	17.28412	21506	38.54	0.75	24.63	0.30	0.60	0.25	0.13	8.80		lm
N3370-B	161.76774	17.28324	20732	41.55	1.15	24.48	0.27	4.33	0.17	-0.06	8.86		lm
N3370-B	161.76869	17.28313	22612	69.35	1.04	23.83	0.22	0.37	0.14	0.01	8.83		lm
N3370-C	161.77931	17.25660	50670	20.52	0.84	25.50	0.41	2.96	0.13	0.00	8.64	low P	lm
N3370-C	161.77441	17.25595	47059	24.49	0.93	24.95	0.34	1.10	0.31	-0.01	8.68		lm
N3370-C	161.77627	17.25957	47494	24.43	1.22	24.57	0.40	0.07	0.28	-0.01	8.77	rej	lm
N3370-C	161.78015	17.25611	51334	28.79	0.98	24.88	0.32	1.31	0.25	-0.06	8.61		lm
N3370-C	161.77485	17.25741	46992	29.60	0.95	24.94	0.27	2.27	-0.02	-0.03	8.72		lm

Table 4—Continued

Field	$\alpha$ (J2000)	$\delta$ (J2000)	Id	P (days)	$V - I$ (mag)	$F160W$ (mag)	$\sigma$ (mag)	Offset (pix)	Bias (mag)	Phase (mag)	[O/H]	Flag <sup>a</sup>	Src*
N3370-C	161.77587	17.25844	47492	39.41	1.15	24.84	0.22	0.48	0.08	-0.05	8.75		lm
N3370-C	161.77827	17.26024	48903	51.68	1.09	24.76	0.28	0.99	0.09	-0.00	8.74		lm
N3370-C	161.77799	17.26004	48741	96.49	0.96	23.90	0.25	0.44	0.11	-0.01	8.75		lm
N3370-R	161.78414	17.26088	52428	33.48	1.04	24.95	0.32	0.74	0.15	-0.06	8.54		lm
N3370-R	161.78547	17.26580	52279	33.69	1.03	24.93	0.26	0.63	0.13	-0.03	8.48		lm
N3370-G	161.75400	17.28417	2638	17.46	0.76	26.08	0.63	6.05	0.47	0.00	8.71	low P	lm
N3370-G	161.75882	17.28007	8807	23.72	1.04	26.46	0.41	0.87	0.61	-0.08	8.92	rej	lm
N3370-G	161.75875	17.28389	61720	25.43	0.90	26.21	0.47	1.70	0.61	-0.02	8.86	rej	lm
N3370-G	161.75791	17.28025	62219	29.43	1.10	25.25	0.49	1.29	0.61	-0.07	8.89		lm
N3370-G	161.75647	17.28052	5744	27.74	1.06	25.35	0.28	5.16	0.18	-0.09	8.83		lm
N3370-G	161.75620	17.28353	4345	34.07	1.21	25.85	0.31	1.05	0.37	-0.12	8.79	rej	lm
N3370-G	161.75647	17.28320	4710	32.62	1.07	25.30	0.39	0.63	0.39	0.07	8.80		lm
N3370-G	161.75710	17.28387	59919	36.99	0.88	25.22	0.25	3.02	0.21	-0.04	8.81		lm
N3370-G	161.76072	17.28069	10677	35.24	1.11	23.49	0.36	10.5	0.29	-0.00	8.97	rej	lm
N3370-G	161.75713	17.28309	5439	45.82	0.98	23.66	0.28	0.95	0.31	0.05	8.83	rej	lm
N3370-G	161.75761	17.28213	6440	43.94	1.17	24.37	0.28	0.32	0.31	0.08	8.86		lm
N3370-G	161.75980	17.28234	9014	45.10	1.12	24.60	0.27	1.47	0.28	-0.06	8.91		lm
N3370-G	161.75525	17.28084	4367	52.72	1.22	24.94	0.28	0.09	0.05	0.04	8.78		lm
N3370-G	161.75695	17.28274	5361	50.60	0.90	23.99	0.27	0.28	0.05	-0.06	8.83		lm
N3370-G	161.75874	17.28466	6706	64.79	0.96	25.00	0.40	1.65	0.31	0.09	8.84	rej	lm
N3370-G	161.75677	17.28193	5501	62.71	1.26	23.58	0.25	0.24	0.04	0.02	8.83		lm
N3982-B	179.09710	55.12080	9531	25.83	0.87	25.45	0.35	0.76	0.00	-0.11	8.70		psl
N3982-B	179.09800	55.11996	32398	45.43	0.87	24.33	0.19	0.36	0.04	-0.10	8.72		psl
N3982-B	179.10593	55.12011	9075	37.04	0.80	24.32	0.33	8.02	0.23	-0.00	8.97		psl
N3982-B	179.10563	55.11935	9114	53.86	1.07	23.52	0.34	0.73	0.13	-0.09	8.93		psl
N3982-C	179.13277	55.12384	12134	19.08	0.86	24.92	0.67	0.80	0.64	-0.03	8.90		psl
N3982-C	179.13148	55.12278	627	38.86	1.15	24.28	0.39	0.47	0.21	0.00	8.93		psl
N3982-C	179.13803	55.12526	281	40.88	1.31	24.36	0.25	0.52	0.23	0.03	8.72		psl
N3982-C	179.13666	55.12775	43380	44.22	0.99	23.97	0.33	0.21	0.21	0.10	8.77		psl
N3982-G	179.09010	55.12513	32813	30.04	1.16	25.22	0.41	4.81	-0.09	-0.01	8.48		psl
N3982-G	179.08546	55.12250	33304	32.02	0.97	24.56	0.21	0.38	0.11	-0.05	8.32		psl
N3982-R	179.09379	55.10950	9610	38.11	1.23	24.40	0.20	0.24	0.06	-0.13	8.28		psl
N3982-R	179.09561	55.11319	32634	41.00	0.89	24.85	0.34	0.69	0.03	-0.11	8.46		psl
N3982-C	179.13316	55.12718	11942	25.57	1.49	25.28	0.37	1.59	0.56	-0.02	8.89		lm
N3982-R	179.09459	55.11199	9584	61.79	1.16	24.59	0.24	0.48	0.15	-0.07	8.39	rej	lm
N3982-Y	179.12839	55.13052	12782	24.11	1.11	25.47	0.46	1.53	0.85	-0.14	8.99		lm
N3982-Y	179.12240	55.13018	2002	37.57	1.35	22.81	0.37	1.07	0.42	-0.08	9.14	rej	lm
N3982-Y	179.12400	55.12933	1434	75.40	1.86	22.33	0.25	0.69	0.21	-0.06	9.14	rej	lm
N3982-Y	179.13114	55.13153	32	29.53	0.89	23.90	0.50	10.4	0.13	0.00	8.88	rej	ps
N3021-B	147.72778	33.54702	30672	13.92	0.48	25.88	0.37	0.87	0.24	-0.04	8.29	low P	lm
N3021-B	147.73211	33.54878	26946	26.84	0.85	25.04	0.32	0.95	0.22	0.04	8.76		lm
N3021-B	147.72812	33.54750	30428	32.60	0.78	25.03	0.30	1.08	0.17	-0.01	8.37		lm
N3021-B	147.73249	33.54885	26545	39.57	0.87	24.79	0.34	4.08	0.08	0.05	8.79		lm
N3021-C	147.72678	33.55614	32088	25.77	0.98	26.35	0.59	1.79	0.59	-0.03	8.89	rej	lm
N3021-C	147.72586	33.55581	32375	24.01	0.82	24.46	0.45	1.37	0.11	-0.01	8.82	rej	lm

Table 4—Continued

Field	$\alpha$ (J2000)	$\delta$ (J2000)	Id	P (days)	$V - I$ (mag)	$F160W$ (mag)	$\sigma$ (mag)	Offset (pix)	Bias (mag)	Phase (mag)	[O/H]	Flag <sup>a</sup>	Src*
N3021-C	147.72645	33.56000	32380	25.18	0.72	25.27	0.31	0.91	0.08	-0.09	8.69		lm
N3021-C	147.72789	33.55893	31803	37.27	0.89	25.30	0.28	1.04	-0.16	-0.05	8.83		lm
N3021-G	147.74838	33.55002	8621	15.37	0.75	25.94	0.64	3.49	0.70	-0.06	8.94	low P	lm
N3021-G	147.74935	33.55170	8102	18.71	0.62	26.10	0.47	2.77	0.48	0.08	8.90	low P	lm
N3021-G	147.74871	33.55237	8636	24.36	0.72	24.91	0.60	4.36	0.10	-0.02	8.93		lm
N3021-G	147.74791	33.55032	9028	31.89	0.72	24.70	0.32	1.53	0.60	0.13	8.98		lm
N3021-G	147.74757	33.55109	9402	39.77	1.15	23.98	0.33	5.43	0.13	0.12	9.02	rej	lm
N3021-G	147.74740	33.55142	9611	40.49	0.63	25.30	0.49	3.20	0.05	0.05	9.04		lm
N3021-G	147.74683	33.55170	10203	95.91	0.85	24.05	0.25	5.58	0.13	0.00	9.08		lm
N3021-G	147.75116	33.55414	7098	82.66	0.72	24.18	0.25	0.55	0.12	0.00	8.67		lm
N3021-G	147.74734	33.55075	9558	88.18	1.43	23.96	0.25	1.28	0.33	-0.05	9.03		lm
N3021-R	147.73688	33.55930	23149	32.52	0.92	25.59	0.40	2.34	0.37	0.06	8.92		lm
N3021-R	147.73982	33.56093	19817	68.61	1.06	23.47	0.24	0.66	0.18	-0.02	8.61		lm
N1309-B	50.513220	-15.40390	52566	47.41	0.53	24.79	0.43	0.64	0.12	-0.01	8.70		lm
N1309-B	50.513500	-15.39881	52170	47.99	0.97	24.63	0.24	0.39	0.07	-0.01	8.73		lm
N1309-B	50.512020	-15.39909	53187	59.75	0.57	24.91	0.35	0.81	0.14	-0.00	8.68		lm
N1309-B	50.516480	-15.40236	49485	74.19	0.39	23.72	0.37	0.24	-0.05	0.01	8.83		lm
N1309-C	50.535980	-15.41296	6737	25.45	0.71	26.03	0.33	3.53	0.03	0.03	8.77	low P	lm
N1309-C	50.535850	-15.41538	7224	30.90	0.82	25.23	0.31	0.71	0.06	0.09	8.70	low P	lm
N1309-C	50.535240	-15.41099	7989	39.41	0.90	24.70	0.24	1.33	0.17	-0.06	8.85		lm
N1309-C	50.535740	-15.41413	59151	32.61	0.59	24.85	0.22	4.19	0.01	-0.02	8.74	low P	lm
N1309-C	50.537010	-15.41209	4882	48.91	0.76	25.25	0.19	0.11	0.12	-0.05	8.78		lm
N1309-C	50.536060	-15.41233	6542	59.12	0.92	24.57	0.22	0.45	0.12	-0.03	8.79		lm
N1309-C	50.535980	-15.41154	6581	58.98	0.79	24.82	0.22	0.36	0.11	0.12	8.82		lm
N1309-C	50.535540	-15.41410	7702	73.76	0.86	24.36	0.25	0.06	0.18	-0.04	8.74		lm
N1309-G	50.540170	-15.39411	2032	42.53	0.72	24.91	0.26	0.74	0.11	-0.03	8.85		lm
N1309-G	50.541640	-15.39645	1166	41.11	1.10	24.84	0.44	4.43	-0.23	0.05	8.83		lm
N1309-Y	50.528160	-15.40843	23076	30.66	0.82	25.99	0.49	2.33	0.52	0.00	9.00	low P	lm
N1309-Y	50.525250	-15.40856	30349	33.51	0.61	26.04	0.68	3.78	-0.22	0.00	8.96	rej,low P	lm
N1309-Y	50.531480	-15.40689	15346	46.85	0.81	25.53	0.51	1.63	0.13	0.01	9.04		lm
N1309-Y	50.528240	-15.40865	22918	42.03	0.81	24.97	0.38	0.76	0.54	0.02	8.99		lm
N1309-Y	50.528300	-15.40526	68817	49.93	0.53	24.63	0.62	10.6	0.40	-0.01	9.11		lm
N1309-Y	50.526610	-15.40578	71911	51.99	0.75	24.07	0.44	4.48	-0.18	-0.02	9.07		lm
N1309-Y	50.526040	-15.40768	28132	52.24	1.00	24.89	0.35	1.29	0.24	0.01	9.00		lm
N1309-Y	50.528080	-15.40923	69494	60.17	0.93	24.97	0.46	6.65	-0.05	-0.00	8.97		lm
N1309-Y	50.529580	-15.40892	19918	64.94	0.80	24.48	0.33	0.26	0.08	0.02	8.98		lm
N1309-Y	50.531070	-15.40794	64757	65.03	1.09	24.27	0.29	1.12	0.24	0.02	9.01		lm
IN-NIC-01	184.68938	47.33554	118961	12.82	1.26	22.58	0.28	0.76	0.16	-0.06	8.90	rej	lm
IN-NIC-02	184.70089	47.34927	110213	11.60	1.18	23.20	0.32	0.71	0.20	-0.01	8.91		lm
IN-NIC-02	184.69963	47.35114	113982	11.64	0.84	24.81	0.48	3.12	-0.14	0.04	8.90	rej	lm
IN-NIC-05	184.70311	47.31951	83857	28.13	0.76	22.05	0.25	4.61	0.32	-0.04	8.93		lm
IN-NIC-05	184.70506	47.32093	80885	65.23	1.13	20.91	0.20	0.32	0.14	-0.07	8.94		lm
IN-NIC-06	184.70488	47.33184	91209	10.80	0.88	23.59	0.37	1.14	0.35	-0.09	8.94		lm
IN-NIC-06	184.70320	47.32795	91129	11.16	1.00	23.25	0.39	1.40	0.40	-0.03	8.93		lm
IN-NIC-07	184.71071	47.34988	95403	11.58	1.03	24.41	0.56	0.99	0.38	-0.00	8.91	rej	lm

Table 4—Continued

Field	$\alpha$ (J2000)	$\delta$ (J2000)	Id	P (days)	$V - I$ (mag)	$F160W$ (mag)	$\sigma$ (mag)	Offset (pix)	Bias (mag)	Phase (mag)	[O/H]	Flag <sup>a</sup>	Src*
IN-NIC-07	184.70793	47.34997	100093	12.02	0.71	24.78	0.59	7.06	0.82	0.12	8.91	rej	lm
IN-NIC-08	184.71066	47.31184	57246	10.90	0.89	22.91	0.63	0.33	0.66	-0.05	8.94	rej	lm
IN-NIC-08	184.71169	47.30965	51416	11.09	0.77	22.81	0.44	5.43	0.40	0.06	8.94	rej	lm
IN-NIC-08	184.71509	47.31114	43119	23.81	0.85	22.56	0.32	5.17	0.65	0.15	8.96		lm
IN-NIC-08	184.71112	47.31241	56661	23.83	0.68	23.04	0.36	0.22	0.05	-0.09	8.94		lm
IN-NIC-08	184.71746	47.31136	36357	29.48	0.86	22.33	0.43	1.78	0.11	-0.10	8.96		lm
IN-NIC-08	184.71239	47.30964	49279	36.12	0.94	21.44	0.19	1.74	0.03	0.27	8.94		lm
IN-NIC-08	184.71440	47.31272	47358	50.89	0.85	21.63	0.20	0.30	0.16	-0.04	8.96		lm
IN-NIC-08	184.71707	47.31160	37841	66.89	1.13	21.61	0.25	0.89	0.21	0.02	8.96		lm
IN-NIC-08	184.71324	47.31224	50193	93.23	0.83	21.17	0.25	0.34	0.06	-0.00	8.95		lm
IN-NIC-08	184.71528	47.31138	42837	95.92	0.93	20.93	0.25	0.34	0.14	0.03	8.96		lm
IN-NIC-09	184.71932	47.31409	34408	22.42	0.85	22.18	0.43	0.63	0.49	-0.08	8.97		lm
IN-NIC-09	184.71746	47.31136	36357	29.48	0.86	22.16	0.29	0.58	0.42	-0.04	8.96		lm
IN-NIC-09	184.71962	47.31407	33434	34.48	0.78	20.99	0.38	0.98	0.20	-0.01	8.98	rej	lm
IN-NIC-09	184.72344	47.31211	19435	39.53	0.82	20.70	0.33	0.39	0.18	-0.00	8.99	rej	lm
IN-NIC-09	184.71707	47.31160	37841	66.89	1.13	21.48	0.25	6.30	0.79	-0.10	8.96		lm
IN-NIC-10	184.72821	47.31332	6616	16.99	0.93	22.83	0.37	5.96	0.64	0.02	9.00		lm
IN-NIC-10	184.72937	47.31691	8052	20.76	0.90	22.17	0.49	6.21	0.23	0.02	9.00		lm
IN-NIC-10	184.72616	47.31461	14643	22.04	1.92	22.05	0.63	2.99	-0.30	-0.04	8.99		lm
IN-NIC-10	184.72389	47.31625	23741	22.68	1.43	22.77	0.32	1.78	0.03	-0.16	8.99		lm
IN-NIC-10	184.72948	47.31746	8361	23.79	1.22	21.97	0.33	0.89	0.35	0.11	8.99		lm
IN-NIC-10	184.72728	47.31776	15470	50.70	1.48	22.19	0.41	1.83	0.24	-0.04	8.99		lm
IN-NIC-10	184.72834	47.31586	9633	69.46	1.19	20.75	0.26	0.48	0.12	0.13	9.00		lm
IN-NIC-11	184.72657	47.34519	54398	15.73	1.06	22.48	0.50	1.82	0.47	0.10	8.91	rej	lm
IN-NIC-12	184.72567	47.32182	25760	9.979	0.92	24.06	0.44	5.12	0.69	-0.07	8.98		lm
IN-NIC-12	184.72505	47.32063	25811	10.30	0.90	23.26	0.68	2.82	0.37	-0.07	8.98		lm
IN-NIC-12	184.72545	47.32166	26176	18.28	1.67	22.49	0.59	0.46	0.15	0.21	8.98		lm
IN-NIC-12	184.72759	47.31971	17151	22.35	1.65	22.46	0.39	0.08	0.47	-0.10	8.99		lm
IN-NIC-12	184.72948	47.31746	8361	23.79	1.22	22.41	0.40	0.98	0.35	-0.01	8.99		lm
IN-NIC-12	184.73086	47.32120	9241	27.25	0.72	22.96	0.47	3.40	0.57	-0.01	8.98		lm
IN-NIC-12	184.73086	47.32065	8480	37.63	0.76	21.29	0.26	0.36	0.04	-0.08	8.98	rej	lm
IN-NIC-12	184.72728	47.31776	15470	50.70	1.48	22.49	0.28	2.30	0.42	-0.06	8.99	rej	lm
IN-NIC-01	184.68739	47.33468	121078	18.42	0.97	22.61	0.21	0.55	0.00	0.18	8.89		lm
IN-NIC-01	184.69005	47.33265	116159	21.87	0.89	23.09	0.21	0.17	0.11	-0.13	8.90		lm
IN-NIC-02	184.70103	47.35073	111064	14.59	0.98	22.99	0.34	2.11	0.30	0.16	8.90		lm
IN-NIC-05	184.70263	47.31955	84934	15.64	0.97	23.35	0.45	1.28	0.42	-0.12	8.93		lm
IN-NIC-05	184.70646	47.32085	77610	42.82	1.00	22.14	0.25	0.71	0.17	-0.15	8.94		lm
IN-NIC-06	184.70453	47.32912	89618	12.47	1.01	23.06	0.31	0.77	0.39	-0.01	8.94		lm
IN-NIC-06	184.70347	47.33143	93585	18.19	0.97	22.90	0.36	1.15	0.48	-0.00	8.93		lm
IN-NIC-07	184.70981	47.35380	99783	14.31	0.80	23.68	0.35	3.80	0.13	0.14	8.90		lm
IN-NIC-07	184.71165	47.35150	95003	20.57	1.21	23.00	0.26	0.78	0.14	0.23	8.90		lm
IN-NIC-07	184.70864	47.35115	99756	29.05	1.04	22.70	0.23	0.59	0.10	-0.00	8.90		lm
IN-NIC-08	184.71348	47.31023	46762	12.65	0.71	23.65	0.56	6.64	-0.38	-0.02	8.95		lm
IN-NIC-08	184.71404	47.31339	49332	16.00	0.71	23.63	0.68	5.62	0.45	0.10	8.96		lm
IN-NIC-08	184.71249	47.31037	49942	16.34	1.03	23.68	0.39	0.63	0.62	-0.03	8.95		lm

Table 4—Continued

Field	$\alpha$ (J2000)	$\delta$ (J2000)	Id	P (days)	$V - I$ (mag)	$F160W$ (mag)	$\sigma$ (mag)	Offset (pix)	Bias (mag)	Phase (mag)	[O/H]	Flag <sup>a</sup>	Src*
IN-NIC-08	184.71407	47.31168	46945	25.12	0.90	22.83	0.31	0.61	0.35	-0.00	8.95		lm
IN-NIC-08	184.71470	47.30831	189390	34.41	0.95	21.96	0.22	0.27	0.02	-0.02	8.95		lm
IN-NIC-09	184.71988	47.31322	31615	23.98	1.32	22.07	0.45	2.34	0.40	0.22	8.98		lm
IN-NIC-09	184.72036	47.31321	30136	26.07	1.22	22.36	0.40	1.02	0.35	-0.13	8.98		lm
IN-NIC-09	184.72467	47.31105	14316	29.63	1.13	22.26	0.50	2.13	0.08	0.11	8.99		lm
IN-NIC-09	184.72402	47.31193	17423	34.57	1.28	22.79	0.33	1.54	0.19	0.24	8.99		lm
IN-NIC-09	184.72228	47.31203	22927	33.99	1.04	22.70	0.49	2.72	-0.09	0.19	8.98		lm
IN-NIC-09	184.71972	47.31095	29058	40.54	0.95	22.56	0.32	4.97	-0.28	-0.19	8.97		lm
IN-NIC-09	184.71854	47.31213	34159	41.57	1.01	21.91	0.24	0.38	0.13	-0.17	8.97		lm
IN-NIC-10	184.72694	47.31762	16299	12.28	1.28	22.86	0.53	6.31	0.54	0.17	8.99		lm
IN-NIC-10	184.72795	47.31605	11066	15.91	1.21	23.80	0.65	13.7	0.60	0.16	9.00		lm
IN-NIC-10	184.72657	47.31756	17357	22.45	1.21	22.39	0.58	4.39	-0.11	-0.06	8.99		lm
IN-NIC-10	184.72375	47.31687	24960	25.49	1.06	22.19	0.50	5.02	0.14	-0.07	8.99		lm
IN-NIC-12	184.72694	47.31762	16299	12.28	1.28	23.33	0.60	2.37	0.83	0.03	8.99		lm
IN-NIC-12	184.73048	47.31999	8723	35.57	0.96	21.46	0.29	0.33	0.10	0.03	8.99		lm
IN-NIC-13	184.73382	47.33895	24365	22.38	0.93	23.12	0.39	0.59	0.44	-0.10	8.91		lm
IN-NIC-13	184.73069	47.33826	32759	42.31	0.95	22.14	0.26	0.99	0.19	-0.10	8.92		lm
IN-NIC-03	184.69895	47.35497	117710	14.30	0.84	23.56	0.26	0.51	0.21	-0.06	8.89		lm
IN-NIC-03	184.69870	47.35607	118782	25.56	0.89	22.34	0.20	0.41	0.09	-0.03	8.89		lm
IN-NIC-04	184.69961	47.33411	102255	12.25	1.04	24.23	0.42	1.68	0.28	-0.10	8.92	rej	lm
IN-NIC-04	184.69929	47.33694	105183	23.00	1.11	22.85	0.29	1.18	0.26	-0.14	8.92		lm
IN-NIC-04	184.69827	47.33338	104131	22.89	0.87	22.21	0.23	3.02	0.14	0.24	8.92		lm
IN-NIC-04	184.70092	47.33803	103070	24.86	1.12	22.88	0.25	0.47	0.24	-0.05	8.92		lm
NIC-POS10	184.84596	47.24667	310420	45.40	0.86	21.34	0.18	0.17	0.03	0.19	8.74		lm
NIC-POS11	184.83328	47.24912	312665	39.09	0.80	23.20	0.19	0.25	0.05	0.11	8.78	rej	lm
NIC-POS12	184.85726	47.22978	307758	32.40	1.02	22.23	0.18	0.20	0.00	0.22	8.71		lm
NIC-POS13	184.72838	47.36342	999999	92.00	1.00	20.26	0.25	0.23	0.02	0.20	8.84		lm
NIC-POS1	184.70981	47.35380	99783	14.31	0.80	23.41	0.36	5.59	0.16	-0.01	8.90		lm
NIC-POS1	184.71165	47.35150	95003	20.57	1.21	23.24	0.26	0.92	0.13	-0.00	8.90		lm
NIC-POS1	184.70864	47.35115	99756	29.05	1.04	22.38	0.21	0.48	0.06	0.06	8.90		lm
NIC-POS1	184.71263	47.35496	95995	36.79	1.05	22.25	0.21	0.21	-0.00	-0.15	8.89		lm
NIC-POS2	184.71006	47.34746	94632	16.03	1.14	23.17	0.38	2.89	0.02	-0.12	8.91		lm
NIC-POS2	184.70643	47.34573	99411	17.02	0.98	22.97	0.28	0.59	0.16	-0.12	8.92		lm
NIC-POS2	184.70905	47.34317	92950	16.70	1.01	23.39	0.35	0.71	0.09	0.00	8.92		lm
NIC-POS2	184.70773	47.34559	97135	31.78	1.20	22.43	0.28	0.57	0.15	-0.11	8.92		lm
NIC-POS3	184.69961	47.33411	102255	12.25	1.04	23.66	0.30	0.46	0.52	-0.13	8.92		lm
NIC-POS3	184.69929	47.33694	105183	23.00	1.11	22.85	0.28	1.06	0.15	-0.12	8.92		lm
NIC-POS3	184.69827	47.33338	104131	22.89	0.87	22.03	0.25	0.98	0.09	0.21	8.92		lm
NIC-POS3	184.69648	47.33310	106960	28.26	0.97	22.51	0.19	0.40	0.08	0.18	8.92		lm
NIC-POS4	184.70931	47.32443	74725	11.99	0.81	23.18	0.68	0.14	0.15	-0.08	8.95		lm
NIC-POS4	184.71440	47.32211	59576	12.65	1.10	23.43	0.36	7.48	0.70	0.15	8.96		lm
NIC-POS4	184.70898	47.32425	75254	16.52	0.98	23.02	0.26	0.34	0.42	-0.04	8.95		lm
NIC-POS4	184.71341	47.32261	62769	33.02	0.77	21.93	0.25	0.66	0.09	-0.05	8.96		lm
NIC-POS5	184.74252	47.34238	2686	44.05	1.06	21.57	0.19	0.28	0.05	0.10	8.88		lm
NIC-POS6	184.83891	47.17151	107069	83.40	1.58	20.56	0.25	0.06	0.01	-0.10	8.67		lm

## 2.4. Near-Infrared Cepheid Relations

In the  $i$ th galaxy, for a set of Cepheids with periods  $\mathbf{P}$ , with mean magnitudes  $\mathbf{m}_X$ , the pulsation equation leads to a period-luminosity ( $P$ - $L$ ) relation of the form

$$\mathbf{m}_X = zp_{X,i} + b_X \log \mathbf{P}, \quad (1)$$

where  $zp_{X,i}$  is the intercept of the  $P$ - $L$  relation, and  $b_X$  is its slope for passband  $X$ . We will make use of multi-linear regressions to *simultaneously* fit the Cepheid data (and in the next section the SN data) and to propagate the covariance of the data and model to the fitted parameters.

It is convenient to express the  $P$ - $L$  relation for the  $j$ th Cepheid  $j$  in the  $i$ th host as

$$m_{X,i,j} = (zp_{X,i} - zp_{X,4258}) + zp_{X,4258} + b_X \log P_{i,j}. \quad (2)$$

Although the  $H$ -band  $P$ - $L$  relation is expected to be relatively insensitive to metallicity as compared to the visible, where metal-line blanketing influences opacity (Marconi et al. 2005), we will *not assume the LMC slope applies to our more metal-rich Cepheid sample.*<sup>2</sup> Instead, we will determine the slope for the narrow range of solar-like metallicity of our sample.

We rewrite equation (2) in matrix form to allow a single, unknown value of  $b_H$ ,

$$\begin{pmatrix} m_{H_1} \\ m_{H_2} \\ \cdot \\ m_{H_n} \\ m_{H_{4258}} \end{pmatrix} = \begin{pmatrix} 1 & 0 & 0 & 0 & 0 & 0 & 1 & \log P_1 \\ 0 & 1 & 0 & 0 & 0 & 0 & 1 & \log P_2 \\ \cdot & \cdot \\ 0 & 0 & 0 & 0 & 0 & 1 & 1 & \log P_n \\ 0 & 0 & 0 & 0 & 0 & 0 & 1 & \log P_{4258} \end{pmatrix} * \begin{pmatrix} zp_{H,1} - zp_{H,4258} \\ zp_{H,2} - zp_{H,4258} \\ \cdot \\ zp_{H,n} - zp_{H,4258} \\ zp_{H,4258} \\ b_H \end{pmatrix} + n(t) \quad (3)$$

Referring to this matrix equation symbolically as  $\mathbf{y} = \mathbf{L}\mathbf{q}$ , we define:  $\mathbf{y}$  is the column of measured magnitudes,  $\mathbf{L}$  is the 2-dimensional “design matrix” with entries that arrange the operations, and  $\mathbf{q}$  is the set of free parameters. With these definitions and  $\mathbf{C}$  as the matrix of measurement errors, we write the  $\chi^2$  statistic as

$$\chi^2 = (\mathbf{y} - \mathbf{L}\mathbf{q})^T \mathbf{C}^{-1} (\mathbf{y} - \mathbf{L}\mathbf{q}). \quad (4)$$

The minimization of  $\chi^2$  with respect to  $\mathbf{q}$  gives the following expression for the maximum likelihood estimator of  $\mathbf{q}$ :

---

<sup>2</sup>The slope in the  $H$  band,  $b_H$ , has been measured by Persson et al. (2004) to be  $-3.234 \pm 0.042$  based on 88 Cepheids in the LMC. Limiting the sample to 75 variables with  $P > 10$  d yields the same result.

$$\hat{\mathbf{q}} = (\mathbf{L}^T \mathbf{C}^{-1} \mathbf{L})^{-1} \mathbf{L}^T \mathbf{C}^{-1} [\mathbf{y}] \quad (5)$$

The standard errors for the parameters in  $\hat{\mathbf{q}}$  are given by the covariance matrix,  $(\mathbf{L}^T \mathbf{C}^{-1} \mathbf{L})^{-1}$  (Rybick & Press 1992).

The seven individual  $P$ - $L$  relations fitted with a common slope are shown in Figure 11. While 240 Cepheids previously identified in the optical (Riess et al. 2009) could be measured in the NICMOS data, it is apparent from Figure 11 that  $\sim 10\%$  appear as outliers in the relations. This is not surprising as we expect outliers to occur from (1) a complete blend with a bright, red source such as a red giant or (2) objects misidentified as Cepheids in the optical or with the wrong period. To reject these outliers we performed an iterative rejection of objects  $> 0.75$  mag from the  $P$ - $L$  relations, resulting in a reduction of the sample to 209. In the next section we consider the effect of this rejection on the the determination of  $H_0$ .

For the sample we find  $b_H = -3.09 \pm 0.11$ , in good agreement with the value of  $-3.23 \pm 0.04$  from the LMC (Persson et al. 2004).

To determine the difference in distances between the anchor galaxy and the SN hosts we now account for interstellar extinction of the Cepheids. Although such extinction is a factor of  $\sim 5$  smaller in the  $H$  band than in the optical and might be ignored (an option we consider in §4), the difference in what remains directly impacts the determination of  $H_0$  at the few percent level.

The use of two or more passbands allows for the measurement of reddening and the associated correction for extinction. For each Cepheid we use the measurement of its mean  $V - I$  color from WFPC2 or ACS. Following Madore (1982) we define a “Wesenheit reddening-free” mean magnitude,

$$\mathbf{m}_W = \mathbf{m}_H - R(\mathbf{m}_V - \mathbf{m}_I), \quad (6)$$

where  $R \equiv A_H / (A_V - A_I)$ . For a Cardelli et al. (1989) reddening law and a Galactic-like value of  $R_V = 3.1$ ,  $R = 0.479$ . In the next section we consider the sensitivity of  $H_0$  to the value of  $R_V$ .

To account for possible differences in the Cepheid photometry measured with ACS and WFPC2, we compared the photometry of 8711 non-variable stellar sources in the field of NGC 3982 observed with both cameras through  $F555W$  and  $F814W$ . Using the master catalog of WFPC2 photometry used by Gibson et al. (2000) and Stetson & Gibson (2001) we find the mean difference between our WFPC2 and ACS  $V - I$  colors of these sources to be  $0.054 \pm 0.005$  mag (WFPC2 is bluer), with no dependence on source color or magnitude. The origin of this difference largely resides in the specific zeropoints adopted by Stetson & Gibson (2001) and those from Riess et al. (2009) and Macri et al. (2006,2009). Because our goal is limited to placing the WFPC2 Cepheid colors on the same photometric scale as the ACS data to measure distances relative to NGC 4258, we corrected the WFPC2 Cepheid data of Gibson et al. (2000) for NGC 4639, NGC 4536, and NGC 3982 to the ACS color scale. The mean  $V - I$  colors of the Cepheids are given in Table 4. We propagate a *systematic* 0.02 mag error in the difference between  $V - I$  colors measured with WFPC2 and ACS

in the next section, though the net effect on  $m_W$  amounts to only  $0.02R \approx 0.01$  mag.<sup>3</sup>

Substituting the values of  $m_W$  for  $m_H$  in equation (3), we find  $b_W = -3.23 \pm 0.11$ .

Differences in  $zp_W$  between galaxies are equivalent to differences in distances, which follows from equation (1) and  $\mu_0 = m_W - M_W$ . Therefore we can now substitute  $(zp_{W,i} - zp_{W,4258}) = (\mu_{0,i} - \mu_{0,4258})$  to derive reddening-free distances,  $\mu_{0,i}$ , for the SN hosts relative to NGC 4258 from the Cepheids,  $\mu_{0,i} - \mu_{0,4258}$ . The results are given in Table 5, column 6.

To account for the possible dependence of Cepheid magnitude on metallicity even over the narrow range of metallicity in our Cepheid sample, we express  $m_W$  as

$$m_{W,i,j} = (\mu_{0,i} - \mu_{0,4258}) + zp_{W,4258} + b_W \log P_{i,j} + Z_W \Delta \log[\text{O}/\text{H}]_{i,j}, \quad (7)$$

where the individual values of  $\Delta \log[\text{O}/\text{H}]_{i,j}$  were derived from the metallicity values and gradients for the Cepheid hosts given by Riess et al. (2009). These values are listed in Table 4.

For the parameter  $Z_W$  we find  $-0.27 \pm 0.18$  in the sense that metal-rich Cepheids have a brighter value of  $m_W$ , though this relation is not significant. Indeed, the benefit of using Cepheids across the distance ladder with similar metallicities is that, as shown in the next section, their relative distance measures are insensitive to the uncertainty in their metallicity relation.

We now move to the joint use of the Cepheid and SN Ia data for deriving the Hubble constant.

### 3. Measuring the Hubble Constant

#### 3.1. Type Ia Supernova Magnitudes

Distance estimates from SN Ia light curves are derived from the luminosity distance,

$$d_L = \left( \frac{L}{4\pi\mathcal{F}} \right)^{\frac{1}{2}}, \quad (8)$$

where  $L$  and  $\mathcal{F}$  are the intrinsic luminosity and the absorption-free flux within a given passband, respectively. Equivalently, logarithmic measures of the flux in passband (e.g.,  $V$ ) (apparent magnitude,  $m_V$ ) and luminosity (absolute magnitude,  $M_V$ ) are used to derive extinction-corrected distance moduli,

---

<sup>3</sup>For analysis using the optical relation  $m_W = m_V - 2.45(m_V - m_I)$ , differences in color measurements between different photometric systems are  $\sim 5$  times larger with additional uncertainties due to the difficulty in cross-calibrating ground-based and space-based systems. The resulting systematic uncertainty is typically 0.10 mag, one of the leading systematic errors in the determination of  $H_0$ .

$$\mu_0 = m_V^0 - M_V^0 = 5 \log d_L + 25 \quad (9)$$

( $d_L$  in units of Mpc), where  $m_V^0$  derives from  $m_V$  corrected for selective absorption through the use of colors and a reddening law.

We may relate the observables of SN Ia distance and redshift,  $z$ , to the scale factor of the Universe,  $a$ , by expanding  $a(t)$  using the definitions

$$H(t) = +\dot{a}/a, q(t) = -(\ddot{a}/a)(\dot{a}/a)^{-2}, j(t) = +(\dot{\ddot{a}}/a)(\dot{a}/a)^{-3} \quad (10)$$

(cf. Visser 2004).

For  $z \approx 0$

$$d_l = \frac{cz}{H_0}, \quad (11)$$

where  $H_0$  is the present expansion rate ( $z = 0$ ) of the Universe.

Allowing for changes in the expansion rate at  $z > 0$

$$d_L(z) = \frac{cz}{H_0} \left\{ 1 + \frac{1}{2} [1 - q_0] z - \frac{1}{6} [1 - q_0 - 3q_0^2 + j_0] z^2 + O(z^3) \right\} \quad (12)$$

or

$$\mu_0 = m_V^0 - M_V^0 = 5 \log \frac{cz}{H_0} \left\{ 1 + \frac{1}{2} [1 - q_0] z - \frac{1}{6} [1 - q_0 - 3q_0^2 + j_0] z^2 + O(z^3) \right\} + 25, \quad (13)$$

Using empirical relations between SN Ia light curve shape and luminosity allows for a modest correction of individual SN Ia magnitudes to relate them to a fiducial luminosity,  $M_V^0$ , at a fiducial epoch (by convention,  $B$ -band peak). For the multi-color light-curve shape (MLCS; Riess et al. 1996) method of fitting SN Ia light curves,  $M_V^0$  is the  $V$ -band peak absolute magnitude for a SN Ia matching the template light curve shape (i.e., the light curve parameter  $\Delta = 0$ ). The value  $m_V^0$  is the maximum light apparent  $V$ -band brightness of the fiducial SN Ia at the time of  $B$ -band peak if it had  $A_V = 0$  and  $\Delta = 0$ . This quantity is determined from a full light-curve fit, so that it is a weighted average, not a measurement at a single epoch.

We can rewrite equation (13) to move the intercept of the magnitude-redshift relation to the left,

$$\log cz \left\{ 1 + \frac{1}{2} [1 - q_0] z - \frac{1}{6} [1 - q_0 - 3q_0^2 + j_0] z^2 + O(z^3) \right\} - 0.2m_V^0 = \log H_0 - 0.2 M_V^0 - 5, \quad (14)$$

and define the intercept of the  $\log cz - 0.2m_V^0$  relation,  $a_v$ ,

$$a_v = \log cz \left\{ 1 + \frac{1}{2} [1 - q_0] z - \frac{1}{6} [1 - q_0 - 3q_0^2 + j_0] z^2 + O(z^3) \right\} - 0.2m_V^0. \quad (15)$$

The intercept,  $a_v$ , is an apparent quantity which is measured from the set of  $(z, m_V^0)$  independent of any absolute (i.e., luminosity or distance) scale. We use the kinematic expansion of  $a_v$  to include terms of order  $z^2$  and  $z^3$  rather than the Friedmann relation (i.e.,  $\Omega_M$ ,  $\Omega_\Lambda$  or  $w = P/(\rho c^2)$ ) to retain its conventional definition (and measurement) as an apparent (not inferred) quantity. In practice the difference between the kinematic and Friedmann relations is negligible in the range  $z < 0.1$  where we determine  $a_v$ .<sup>4</sup>

Figure 12 shows a Hubble diagram for 240 SNe Ia from Hicken et al. (2009) whose intercept determines the value of  $a_v$ . The magnitude- $z$  relation was determined with the fiducial parameters in MLCS2k2 (Jha et al. 2007). Limiting the sample to  $0.023 < z < 0.1$  (to avoid the possibility of a local, coherent flow) leaves 140 SNe Ia where  $z$  is the redshift in the restframe of the CMB, the present acceleration  $q_0 = -0.55$  and prior deceleration  $j_0 = 1$  (Riess et al. 2007) yields  $a_v = 0.698 \pm 0.00225$ . The sensitivities of  $a_v$  to the cosmological model, the minimum redshift and the MLCS2k2 parameters are discussed in the next section.

For the  $i$ th member of a set of nearby SNe Ia whose luminosities are calibrated by independent estimates of the distances to their hosts, the Hubble constant is given from equation (14) and (15) as

$$\log H_0^i = \frac{(m_{v,i}^0 - \mu_{0,i}) + 5a_v + 25}{5}. \quad (16)$$

The terms  $\mu_{0,i}$ , determined from Cepheid data, were discussed in the previous section (e.g., equation (7)).

Because the selection of the fiducial SN Ia along the luminosity vs. light-curve shape relation is arbitrary, the value of  $a_v$  is also arbitrary. However, the inferred value of  $H_0$  is independent of this choice because the luminosity of the fiducial cancels in the sum  $m_{v,i}^0 + 5a_v$  in equation (16). For each SN Ia, the sum  $m_{v,i}^0 + 5a_v$  in equation (16) is a *fundamental* measure of its distance (in magnitudes) in the sense that it is independent, in principle, of the various approaches used to relate SN Ia light curves and their luminosity. It is also independent of bandpass. This sum makes it clear that the measurement of  $H_0$  depends only on the apparent *differences* between SN Ia distances in the calibration set and the Hubble-flow set.<sup>5</sup> Systematic errors may arise from a

---

<sup>4</sup>It is worth noting that terms of order  $z^2$  were not included in the use of  $a_v$  and SNe Ia by Freedman et al. (2001) from Suntzeff et al. (1999) and Phillips et al. (1999), tantamount to setting  $q_0 = 1$  or  $\Omega_M = 2$  and reducing  $H_0$  by  $\sim 3\%$ .

<sup>5</sup>This SN difference measurement is similar to the way SNe are used at high redshift to measure dark energy, but

combination of inaccuracies in the light-curve fitter and differences in the mean properties of the calibration and Hubble-flow samples. We will explore the size of these errors in the next subsection by varying the assumptions of the light-curve fitter and by using a different one, SALT II (Guy et al. 2005).

In Table 5 we give the quantities  $m_{v,i}^0 + 5a_v$  for each of the SHOES SNe Ia.

In Figure 13 we compare the relative distances determined strictly from Cepheids,  $\mu_{0,i} - \mu_{0,4258}$ , and from SNe Ia,  $m_{v,i}^0 + 5a_v$ . These quantities are relative in the sense that they both involve purely differential measurements of like quantities and benefit from the cancellation of systematic errors associated with the determination of absolute quantities. The dispersion between these relative distances is 0.08 mag, somewhat smaller than the mean SN distance error of 0.11 mag.

### 3.2. Global Fit for $H_0$

For convenience we define a parameter ( $m_{v,4258}^0$ ) which is the expected reddening-free, fiducial, peak magnitude of a SN Ia appearing in NGC 4258. We then express  $m_v^0$  for the  $i$ th SN Ia as

$$m_{v,i}^0 = (\mu_{0,i} - \mu_{0,4258}) + m_{v,4258}^0. \quad (17)$$

Combining the two equations for apparent magnitudes; for SNe Ia, equation (17), and for Cepheids, equation (7), we write one matrix equation,

---

without the complexity of significant SN evolution, reddening-law evolution,  $K$ -corrections, time dilation changes in demographics, or gravitational lensing.

$$\begin{pmatrix} m_{w,1,1} \\ m_{w,1,2} \\ \dots \\ m_{w,1,r_1} \\ m_{w,2,1} \\ \dots \\ m_{w,2,r_2} \\ \dots \\ m_{w,n,1} \\ \dots \\ m_{w,n,r_n} \\ m_{w,4258,1} \\ \dots \\ m_{w,4258,r_0} \\ m_{v,1}^0 \\ m_{v,2}^0 \\ \dots \\ m_{v,n}^0 \end{pmatrix} = \begin{pmatrix} 1 & 0 & \dots & 0 & 1 & \log P_{1,1} & 0 & \Delta \log [O/H]_{1,1} \\ 1 & 0 & \dots & 0 & 1 & \log P_{1,2} & 0 & \Delta \log [O/H]_{1,2} \\ \dots & \dots \\ 1 & 0 & \dots & 0 & 1 & \log P_{1,r_1} & 0 & \Delta \log [O/H]_{1,r_1} \\ 0 & 1 & \dots & 0 & 1 & \log P_{2,1} & 0 & \Delta \log [O/H]_{2,1} \\ \dots & \dots \\ 0 & 1 & \dots & 0 & 1 & \log P_{2,r_2} & 0 & \Delta \log [O/H]_{2,r_2} \\ \dots & \dots \\ 0 & 0 & \dots & 1 & 1 & \log P_{n,1} & 0 & \Delta \log [O/H]_{n,1} \\ \dots & \dots \\ 0 & 0 & \dots & 1 & 1 & \log P_{n,r_n} & 0 & \Delta \log [O/H]_{n,r_n} \\ 0 & 0 & \dots & 0 & 1 & \log P_{4258,1} & 0 & \Delta \log [O/H]_{4258,1} \\ \dots & \dots \\ 0 & 0 & \dots & 0 & 1 & \log P_{4258,r_0} & 0 & \Delta \log [O/H]_{4258,r_0} \\ 1 & 0 & \dots & 0 & 0 & 0 & 1 & 0 \\ 0 & 1 & \dots & 0 & 0 & 0 & 1 & 0 \\ \dots & \dots \\ 0 & 0 & \dots & 1 & 0 & 0 & 1 & 0 \end{pmatrix} * \begin{pmatrix} \mu_{0,1} - \mu_{0,4258} \\ \mu_{0,2} - \mu_{0,4258} \\ \dots \\ \mu_{0,n} - \mu_{0,4258} \\ z p_{w,4258} \\ b_W \\ m_{v,4258}^0 \\ Z_W \end{pmatrix} + \text{noise}, \quad (18)$$

for  $n$  SN host galaxies ( $n = 0$  will correspond to NGC 4258), with host  $i$  having  $r_i$  Cepheids. Thus we have  $t = n + \sum_{i=0}^n r_i$  equations to solve simultaneously. The only term of significance for the determination of  $H_0$  is  $m_{v,4258}^0$  and its uncertainty derived from the covariance matrix of fitted parameters, which propagates the uncertainties in Cepheid nuisance parameters such as the slope and metallicity relations for the Cepheid.<sup>6</sup> The meaning of  $m_{v,4258}^0$  can be readily seen from Figure 13 as it connects the Cepheid and SN Ia relative distance measures, i.e.,  $m_{v,i}^0 = m_{v,i}^0 - (\mu_{0,i} - \mu_{0,4258})$ .

From equation (16) we derive our best estimate of  $H_0$  using

$$\log H_0 = \frac{(m_{v,4258}^0 - \mu_{0,4258}) + 5a_V + 25}{5}. \quad (19)$$

Derived this way, the full statistical error in  $H_0$  is the quadrature sum of the uncertainty in the three *independent* terms ( $\mu_{0,4258}$ ,  $m_{v,4258}^0$ , and  $5a_V$ ) where  $\mu_{0,4258}$  is the previously discussed geometric distance estimate to NGC 4258 (Herrnstein et al. 1999, Humphreys et al. 2009). More than a decade of tracking the Keplerian motion of its water masers supports an uncertainty of 3% ( $\sigma = 0.06\text{mag}$ ; Humphreys et al. 2008, 2009, Greenhill et al. 2009).

Our result is  $H_0 = 74.2 \pm 3.4 \text{ km s}^{-1} \text{ Mpc}^{-1}$ , a 4.6% measurement. The uncertainty from the terms independent of the maser distance to NGC 4258, e.g., errors due to the form of the

---

<sup>6</sup>However, unlike one such real event, the precision of our estimate of  $m_{v,4258}^0$  is equivalent to measuring  $n$  such SN Ia events (requiring a millennium to accomplish!), though modestly diminished by the noise in the Cepheids measurements.

$P$ - $L$  relation, metallicity dependences, photometry bias, and zeropoint errors result in a  $\pm 3.4\%$  uncertainty in  $H_0$ . In past determinations of the Hubble constant, these sources of uncertainty have been the leading systematic uncertainties. In this analysis, these uncertainties have been reduced by matching the distribution of Cepheid measurements (i.e., metallicity, periods, and photometric systems) between NGC 4258 and the SN hosts. However, given the small uncertainty in  $H_0$ , it is important to consider a broader exploration of systematic uncertainties of the type now under examination for large-scale high-redshift SN Ia surveys (e.g., Astier et al. 2006; Wood-Vasey et al. 2007; Sullivan et al. 2007).

## 4. Systematics

In Table 6 we show 22 variants of the previously described analysis which we use to estimate the systematic error on our measurement of  $H_0$ . Our primary analysis in row 1 of Table 6 is based on our estimation of the best approach. Column (1) gives the value of  $\chi^2_\nu$ , column (2) the number of Cepheids in the fit, column (3) the value and total uncertainty in  $H_0$ , and column (4) the uncertainty without including the uncertainty in the maser distance for NGC 4258. Column (5) gives the determination of  $M_V^0$ , a parameter specific to the light curve fitter employed, column (6) the value and uncertainty in the metallicity dependence, and column (7) the value and uncertainty of the slope of the Cepheid  $P$ - $L$  or  $P$ - $W$  relation. The next seven parameters are used to indicate variants in the analysis whose impact we now consider.

### 4.1. SN Systematics

Following Wood-Vasey et al. (2007), the leading sources of systematic uncertainty in the cosmological use of SNe Ia relevant to our analysis are addressed here.

*Lower Limit in SN redshift used to measure Hubble flow:* The minimum redshift beyond which SNe Ia measure the Hubble flow has been an ongoing source of debate. Zehavi et al. (1998) and later Jha et al. (2006) claimed to see a local “Hubble bubble” with an increased outflow of  $\sim 5\%$  within a local void ending at  $z = 0.023$ . Conley et al. (2007) demonstrated that the evidence for the bubble rested on a set of SNe Ia at  $0.01 < z < 0.023$  with more than average reddening and that the reality of the bubble depended on the form of their extinction, whether  $R_V$  is Galactic in nature ( $R_V = 3.1$ ) or empirically determined by minimizing the scatter in the Hubble flow ( $R_V = 2$  to 2.5). We consider both approaches to estimating the extinction in the range of  $0.01 < z < 0.023$  when we consider the value of  $R_V$  used for the SNe.

We think the safest choice is to begin the measurement of the Hubble flow at  $z > 0.023$  to avoid the uncertainty of the Bubble or other coherent large-scale flows. A number of authors (Hui & Greene 2006; Cooray & Caldwell 2006) have shown that coherent flows like a Hubble bubble are likely to induce bias at lower redshifts, and we maintain our view that it is better to

restrict our analysis to  $z > 0.023$  and avoid this possible bias. The penalty is a reduction in the statistical precision of the measurement of the Hubble flow, but this term remains subdominant in the determination of  $H_0$ . However, we also include a number of analyses with  $z_{\min} = 0.01$ , as indicated by column (8) of Table 6. These have the effect of raising the Hubble constant by 1.0 to  $1.2 \text{ km s}^{-1} \text{ Mpc}^{-1}$  depending on the aforementioned treatment of extinction. An alternate selection of the Hubble flow set would be to consider all SNe Ia at  $z > 0.01$  but limit the selection to those with  $A_V < 0.5$ , making the Hubble flow sample a good match to the calibrators and avoiding the degeneracy between the Hubble Bubble and the extinction law at  $z < 0.023$ . This approach results in a value of  $H_0$  from SNe Ia at  $z > 0.01$  which is only  $0.7 \text{ km s}^{-1} \text{ Mpc}^{-1}$  greater than the nominal fit at  $z > 0.023$ .

*SN-host  $R_V$ :* In our primary analysis we account for the difference in SN Ia extinction between the calibration and Hubble-flow samples using the  $UBVRI$  colors of the SNe and the MLCS2k2 prescription. For the extinction due to host-galaxy dust our primary analysis uses a recent “consensus” value of  $R_V = 2.5$  (fit parameter 37 in column 9 of Table 6) for the lines of sight of SNe Ia (Kessler et al. 2009), but we also consider values for  $R_V$  of 1.5, 2.0, and 3.1 with fit parameters of 29, 28, and 20, respectively. The change in  $H_0$  is  $0.2 \text{ km s}^{-1} \text{ Mpc}^{-1}$  across the range of  $1.5 < R_V < 3.1$  for the SNe. The effect is so small because the SN colors for the calibration sample and those in our nominal Hubble-flow sample are well matched, so altering  $R_V$  for the SNe provides little change.

*Distribution of host-galaxy extinction:* The observed distribution of SN Ia host galaxy extinction is used as a prior in the determination of the extinction of individual SNe Ia (Riess, Press, Kirshner 1996) and is particularly important in the absence of precise color measurements (e.g., at high redshifts). However, the prior has little effect on the present analysis because the SN colors at low redshifts are well measured. To determine the sensitivity to this prior, we varied its functional form across two extremes, using either a simulation of the lines-of-sight through galaxies (Deaton, Branch, Fisher 1998; “glos”) which anticipates less extinction on average than the default or no extinction prior at all, (fit parameters 27 and 26), respectively. The difference in  $H_0$  is only  $0.8 \text{ km s}^{-1} \text{ Mpc}^{-1}$ . We also changed the algorithm used to fit and compare the SN Ia light and color curves from MLCS2k2 to the SALT II (Guy et al. 2005) approach. These fits (fit parameter 42) reduce  $H_0$  by  $0.5 \text{ km s}^{-1} \text{ Mpc}^{-1}$  with other variants held fixed. Overall we find the determination of  $H_0$  is insensitive to assumptions about the relation between SN Ia colors and extinction.

*SN Ia  $U$ -band:* We also perform an analysis of the SN data discarding the  $U$  band, fit 61, as it should be most sensitive to the form of the extinction law, changes in SN Ia metallicity, and errors in calibration. This decreases  $H_0$  by  $1.0 \text{ km s}^{-1} \text{ Mpc}^{-1}$ . Because both the nearby and Hubble flow samples make use of the same  $U$ -band calibration (Jha et al. 2005), our results are insensitive to the parameters of the  $U$ -band (Kessler et al. 2009).

Other sources of systematic error listed in Wood-Vasey et al (2007) arise from a large change in redshift between two samples of SNe Ia (i.e., cross-filter  $K$ -corrections and the possibility of SN Ia evolution) and are not significant in our analysis as all SN data are at  $z < 0.1$ . In general,

changes to the treatment of the SN Ia light curves affect both the calibration and Hubble-flow sample similarly, largely canceling in the sum  $m_v^0 + 5a_v$  and their impact on  $H_0$ .

## 4.2. Cepheid Systematics

For systematic errors relevant to the analysis of Cepheid data, Table 14 in Freedman et al. (2001) lists the dominant terms. The largest terms relevant to our analysis are considered here.

*Cepheid metallicity:* Metallicity was addressed in §3. The critical conclusion is that the range in metallicity for our Cepheid data is small ( $\Delta[O/H] \sim 0.1$ ), a factor of four times smaller than if LMC Cepheids are used to calibrate SNe Ia. In addition, the metallicity sensitivity should be further reduced by a significant factor by observing Cepheids in the near-IR (Marconi et al. 2005). However, we formally include and marginalize over a first-order metallicity dependence for the Cepheids using our previous measurements of the host metallicities. It may be of interest to remove the metallicity term in the analyses to determine its impact on  $H_0$ . We include a few such entries in Table 6, indicated by “– – –” in the entry for this term. The result is that the nominal uncertainty in  $H_0$  decreases by 5% and its value is reduced by  $\sim 1.2$ .

*Cepheid reddening:* Reddening of the Cepheids is largely mitigated over optical-based analyses by the use of  $H$ -band photometry, which reduces the net by a factor of 5 over the  $V$ -band. The use of Wesenheit magnitudes should account for what extinction remains. However, our knowledge of the reddening law is imperfect, perhaps resulting in systematic errors. Previous work has shown that a Galactic value of  $R_V = 3.1$  is appropriate for extragalactic Cepheids (Macri et al. 2001) and this is used in our primary analysis. We also fit the Cepheids with  $R_V = 2.0$  and 2.5 as indicated in Table 6. The result is an increase in  $H_0$  by 0.5 to 1.0  $\text{km s}^{-1} \text{Mpc}^{-1}$  when the value of  $R_V$  for Cepheids is decreased from 3.1 to 2.0. As an alternative, we fit the Cepheids with only their  $H$ -band magnitudes, which increases  $H_0$  by 1.6  $\text{km s}^{-1} \text{Mpc}^{-1}$ , indicating that the differential extinction of the Cepheids in the  $H$  band between NGC 4258 and the SN hosts is  $\sim 0.04$  mag; we think it prudent to account for this difference using the colors of the Cepheids.

*Short-end limit of Cepheid periods:* Because the Cepheids were selected at bluer wavelengths, the bias of selecting brighter Cepheids at shorter periods due to a magnitude limit does not necessarily apply to the  $H$  band magnitudes. The dispersion in magnitude at a given period arising from the width of the instability strip will be significantly reduced in the near-IR as we view Cepheids on their Rayleigh-Jeans tail. In addition, the use of Wesenheit magnitudes mitigates the contribution to the selection bias due to the color variation on the instability strip. However, 11 of the Cepheids used in our primary analysis have periods which are shorter than the low period limits determined in Riess et al. (2009) for the onset of optical selection bias and these are indicated in Figure 11. Rejecting these (resulting in the entry in Table 6 with 199 Cepheids) results in an increase in  $H_0$  of 0.4  $\text{km s}^{-1} \text{Mpc}^{-1}$  and a 2% increase in its uncertainty.

*Other:* Other significant terms in Freedman et al. (2001) include bulk flows, crowding, and ze-

ropoints. We addressed bulk flows in §4.1. Errors due to crowding were discussed in §2.3. The key points regarding crowding are (1) we correct each Cepheid statistically for crowding bias, and (2)  $H_0$  is only sensitive to a *difference* in crowding between NGC 4258 and the SN hosts and (3) artificial-star tests indicate that this difference is only 0.02 mag in the photometry of the Cepheids, even before a statistical correction is applied. To test for any remaining dependence on  $H_0$  on the degree of crowding, we analyzed subsets of Cepheids with the least apparent crowding. We found that truncating the Cepheid sample to the objects in the lower 40%, 50%, or 60% of the crowding bias ( $< 0.12$ ,  $< 0.15$ , or  $< 0.20$  mag) results in a reduction in the Hubble constant by 2.7%, 3.2% and 0.1%, respectively. The overall uncertainty in  $H_0$  naturally increases as the Cepheid sample is reduced, rising by 25% when retaining only 40% of the original sample. Thus we find the net effect on  $H_0$  due to crowding is contained within the statistical uncertainties.<sup>7</sup> This is an advantage of the use of NGC 4258 over the LMC and the Galaxy, as this and other difficulties in achieving accurate photometry of Cepheids (such as the determination of photometric zeropoints) largely cancel in the determination of  $H_0$ .

We also consider the effect on  $H_0$  of the rejection of outliers on the Cepheid  $P$ - $L$  relations discussed in §2.4. Including the rejected objects naturally has a severe impact on the value of  $\chi^2_\nu$  (where  $\nu$  is the number of degrees of freedom), increasing it from 0.84 to 1.38, with each rejected object contributing an average of  $\chi^2 = 5$ . This variant is indicated in Table 6 by the increase in the sample of Cepheids from 209 to 240. The change in  $H_0$  is an increase of  $3 \text{ km s}^{-1} \text{ Mpc}^{-1}$ , the largest change, but still within the  $1\sigma$  of the statistical error. However, as discussed in §2.4, such outliers are expected and we think it is sensible to reject them as they may pull the global solution well beyond their merit. They are included in Table 4 for those who want to consider them further. We also considered a less stringent outlier cut of  $\pm 1.0$  mag resulting in the retention of 228 out of 240 Cepheids, increasing  $H_0$  by  $1.3 \text{ km s}^{-1} \text{ Mpc}^{-1}$  and demonstrating that most of the change in  $H_0$  results from the most extreme of outliers.

Historically, the determination of  $H_0$  through the Cepheid and SN Ia distance ladder has been significantly altered by choices made in the analysis, with different authors making different (if all reasonable) choices leading to different results. Thanks to the greater homogeneity of the data we are using and the smaller number of steps needed to proceed from a direct geometric distance determination to the final measurement of  $H_0$ , we could expect a priori that different choices would not have a major impact on our results. We have already shown that no single variant described above causes a significant change in  $H_0$ . However, to propagate the systematic uncertainty from variants in the analysis and to consider *combinations* of analysis variants, we developed a number of plausible scenarios in which different choices are made and the full analysis is completed to determine  $H_0$ . The results are presented in Table 6.

Although systematic errors are notoriously difficult to quantify, our approach is to use the

---

<sup>7</sup>Implicit in this analysis is that local blending of Cepheids with binary companions or cluster companions would also cancel between NGC 4258 and the SN hosts.

variation in  $H_0$  in the previous analyses to determine the systematic error. The variation in the inferred value of  $H_0$  is relatively small, with a median and dispersion of  $74.2 \pm 1.0 \text{ km s}^{-1} \text{ Mpc}^{-1}$ . The median is the same as our primary determination (thus the changes scatter fairly equally between increases and decreases), and all inferred values lie within a range of about  $\pm 3 \text{ km/s/Mpc}$ . We take the formal dispersion of  $1.0 \text{ km/s/Mpc}$  as an estimate of the *systematic* uncertainties in our determination, which we then add in quadrature to the statistical uncertainty of the value derived with our preferred approach, yielding a final estimate of  $H_0 = 74.2 \pm 3.6 \text{ km s}^{-1} \text{ Mpc}^{-1}$ .

### 4.3. Anchor Systematics

The use of NGC 4258 in lieu of the LMC or the Galaxy as an anchor to the distance ladder provides a significant enhancement to the precision and accuracy in the measurement of  $H_0$ . Indeed, a 3% uncertainty in the distance to NGC 4258 does not even dominate the current total uncertainty. The natural advantages of NGC 4258, including the sample size, period range, and typical metallicity of its Cepheids, and the ability to measure them in the same way as those in SN Ia hosts, provide for extensive use of differential measurements of the Cepheids in the distance ladder and the means to measure  $H_0$  to  $< 5\%$ . In the next section we discuss the use of additional maser hosts which can serve to test and improve the maser distance estimates. However, at present there is only one thoroughly measured system, and use of the LMC or the Galaxy as anchors can still provide a test of the distance scale set by NGC 4258.

A set of 10 parallax measurements to Galactic Cepheids was recently obtained by Benedict et al. (2007) using the Fine Guidance Sensor on *HST*. Parallax measurements remain the “gold standard” of distance measurements, and unlike previous HIPPARCOS measurements, the *individual precision* of this set of measurements is high, averaging  $\sigma = 8\%$  for each. We have not made use of additional distance measures to Galactic Cepheids based on the Baade-Wesselink method or stellar associations as they are much more uncertain than well-measured parallaxes, and the former appear to be under refinement due to uncertainties in their projection factors, as discussed by Fouqué et al. (2007) and van Leeuwen et al. (2007).

Considered as a set, the Cepheids in Benedict et al. (2007) have an uncertainty in their mean distance measure of only 2.5%, comparable to the precision of the measurement of NGC 4258. These Galactic Cepheids also have metallicities which are very similar to that of Cepheids in the SN hosts as discussed by Sandage et al. (2006). Using the values of  $\mu_0$  (including corrections for interstellar extinction and Lutz-Kelker-Hanson bias) and  $V, I$ -band magnitudes given by Benedict et al. (2007), as well as  $H$ -band magnitudes compiled by Groenewegen (1999)<sup>8</sup>, we determined the

---

<sup>8</sup>For  $\eta$  Gem and W Sgr we determined  $H = 2.18 \pm 0.05$  and  $2.87 \pm 0.05$ , respectively, based on  $J$  and  $K$  data from Berdnikov et al. (1996).

absolute Wesenheit magnitudes of this set of 10 variables. Their  $P$ - $L$  relation is shown in Figure 11. Their inclusion in the global fit is achieved by altering equation (7) for the NICMOS Cepheids to be

$$m_{W,i,j} = \mu_{0,i} + M_W + b_W \log P_{i,j} + Z_W \Delta \log[\text{O}/\text{H}]_{i,j}, \quad (20)$$

and equation (17) for the SNe Ia to be

$$m_{v,i}^0 = \mu_{0,i} - M_V^0. \quad (21)$$

Moreover, for the Galactic Cepheids,

$$M_{W,i,j} = M_W + b_W \log P_{i,j} + Z_W \Delta \log[\text{O}/\text{H}]_{i,j}, \quad (22)$$

where  $M_W$  is the absolute Wesenheit magnitude for a Cepheid with  $P = 1$  d.

The key parameters in the determination of  $H_0$  change from  $m_{v,4258}^0$  and  $\mu_{0,4258}$  in equation (19) to  $M_V^0$ ,

$$\log H_0 = \frac{M_V^0 + 5a_v + 25}{5}. \quad (23)$$

As before, the statistical error in  $M_V^0$  includes all Cepheid-related uncertainties such as the nuisance parameters like the slope and metallicity relations, and the uncertainty in  $H_0$  comes from the two independent terms ( $M_V^0$ ,  $5a_v$ ). The Cepheids in NGC 4258 still contribute to the global analysis as they help determine the slope of the  $P$ - $L$  relation, though their distance estimate is immaterial to the determination of  $H_0$ . We now include a  $\sigma = 0.04$  mag uncertainty in the photometry (i.e., zeropoints and relative crowding) between the space-based Cepheid data and the ground-based Cepheid data. These analyses are indicated in Table 6 with the scale given as “MW.” Compared to the primary analysis based on the independent distance measurement to NGC 4258, use of the Benedict et al. (2007) parallaxes reduces  $H_0$  by  $0.9 \text{ km s}^{-1} \text{ Mpc}^{-1}$  with an increase in the uncertainty of 15%.

However, there are some “risks” in taking this route over that based on the distance to NGC 4258. The magnitudes of these Galactic Cepheids, unlike the distant Cepheids, suffer little crowding, and so we must fully rely on the statistical crowding corrections of mean 0.16 mag in §2.3 rather than the more modest difference in the correction between NGC 4258 and the SN hosts of 0.02 mag. (We assumed a systematic uncertainty of 0.03 mag for use of the the full corrections.) Errors along the magnitude scale from Galactic Cepheids of  $\langle H \rangle = 2$  mag to those in SN hosts of 25 mag pose another risk in this route. We estimate 0.03 mag systematic uncertainty for the magnitude scale which is included in the values in Table 6. In addition, the mean period of the Benedict et al. (2007) Cepheids,  $\langle P \rangle = 10$  d is significantly lower than the  $\langle P \rangle \approx 35$  d in the SN hosts. The use of the Cepheids in NGC 4258, even without the use of its distance, provides an empirical

bridge across this period range. Still, the assumption of the linearity of the  $P$ - $L$  relation, even in the  $H$  band and even for a Wesenheit relation, is another weakness along this route. We estimate an 0.04 mag systematic uncertainty from this mismatch in mean periods. Including systematics, the total uncertainty in  $H_0$  is 5.8%, only moderately worse than the NGC 4258 route but the result carries more caveats. Future measurements from GAIA of precise parallaxes for  $\sim 10^3$  Cepheids over a wide range of periods will provide increased precision while removing the reliance on the form of the  $P$ - $L$  relation to yield a great improvement to the pursuit of  $H_0$  *if accompanied with more precise calibration of the near-IR magnitude scale*.

The use of the LMC as our anchor for the distance scale carries similar risks as those discussed for Milky Way Cepheids with two significant additions: the metallicity of the LMC differs substantially from the SN hosts and the distance to the LMC is uncertain at the  $> 5\%$  level. Nevertheless, the LMC has a long history of use as an anchor, and for comparison to previous work it is valuable to again cast the LMC in that role. We use the set of  $H$ -band Cepheid measurements from Persson et al. (2004) and the optical measurements of Sebo et al. (2002) to extract the 53 Cepheids with measurements of their mean magnitudes in  $VIH$ . Due to the significant difference in metallicity between the LMC and the SN hosts of  $\Delta[\text{O}/\text{H}] \approx 0.4$  dex and our lack of constraint on or detection of a metallicity parameter, we made no metallicity correction. This approach is supported by theory, in which the zeropoints of near-IR  $P$ - $L$  relations are found to vary with chemical composition by a factor of  $\sim 3$  less than those of optical zeropoints (Marconi et al. 2005). Assuming that for the LMC,  $\mu_0 = 18.42$  mag based on a set of 4 detached eclipsing binaries (Fitzpatrick et al. 2003) and with a generous  $\pm 0.10$  mag uncertainty to allow for the wide range of estimates for the LMC distance, we find  $H_0 = 73.4 \pm 4.65 \text{ km s}^{-1} \text{ Mpc}^{-1}$  as shown in Table 6, in good accord with the previous two anchors.

In summary, we find that a full propagation of statistical error and the inclusion of the systematic error gives  $H_0 = 74.2 \pm 3.6 \text{ km s}^{-1} \text{ Mpc}^{-1}$ , based on the cleanest route through NGC 4258, but also consistent with independent though riskier distance-scale anchors from Milky Way Cepheid parallaxes and the LMC.

#### 4.4. Error Budget

As discussed in §4, our total error is the sum of the uncertainty in the three measured terms on the right-hand side of equation (19) and the systematic error derived from considering alternatives to the primary analysis. To illuminate how error propagates along our (and other) distance ladders, we itemize the contributions in Table 7.

The first term is the distance precision of the anchor, followed by the mean of its set of Cepheids (i.e., the zeropoint of its  $P$ - $L$  relation). The next term is the mean of the set of Cepheids in each SN host and the precision of a single SN, each divided by the number ( $n$ ) of hosts. For this calculation  $n = 6$ . Next is the uncertainty in the SN Ia apparent magnitude vs.  $z$  relation; SNe Ia in the

Hubble flow now provide a Hubble diagram with 240 published SNe Ia out to  $z \approx 0.1$ , yielding an uncertainty of 0.5% Hicken et al. (2009). The next term arises from the uncertainty in the difference between the photometric calibration used to observe Cepheids in the anchor and in the SN hosts in two or more passbands. These photometric calibration errors are then amplified by the need to deredden Cepheids with a reddening law,  $R$ , of size 2.1 and 0.48 for  $VI$  and  $VIH$  Cepheid measurements, respectively. The next two terms arise from the difference in the mean metallicities and the mean periods of the Cepheids in the anchor and hosts, and the uncertainty in their respective correlation with Cepheid luminosity. The last term contains the uncertainty from the photometric anomalies of WFPC2, charge transfer efficiency (CTE), and the “long versus short effect.” (Holtzman et al. 1995).

The reduction in total uncertainty in  $\sigma_{H_0}$  from 10% to 5% is a consequence of a number of improvements along the ladder. Most come from greater homogeneity in zeropoints, metallicity, and periods of the samples of Cepheids collected in the anchor and the SN hosts. Changing from the optical to the near-IR reduces the reddening term,  $R$ , by a factor of 5. NGC 4258 also provides greater distance precision than the LMC, and a larger sample of long-period Cepheids. The recent increase in the sample of SNe Ia at  $0.01 < z < 0.1$  (Hicken et al. 2009) provides a modest improvement.

## 5. Dark Energy

An independent measurement of  $H_0$  is a powerful complement to the measurement of the cosmological term  $\Omega_M H_0^2$  derived from the power spectrum of the CMB. In the context of a flat Universe, the fractional uncertainty in the value of an (assumed constant) equation-of-state parameter ( $w$ ) of dark energy is approximately twice the fractional uncertainty in  $H_0$  ( $\sigma_w \approx 2\sigma_{H_0}$ ), as long as the fractional uncertainty in  $H_0$  is greater than or equal to that in  $\Omega_M H_0^2$  (Hu 2005). A marked improvement in the precision of  $\Omega_M H_0^2$  has been realized in the recent 5-year WMAP analysis from the localization of the third acoustic peak (Komatsu et al. 2008). The result is a model-insensitive measurement of  $\Omega_M H_0^2$  to better than 5% precision.

Using the output of the WMAP 5-year Monte Carlo Markov Chain (MCMC) from Komatsu et al. (2008)<sup>9</sup> in a flat,  $w$ CDM cosmology (i.e., dark energy with constant  $w$ ) yields the degenerate confidence regions in the  $H_0 - w$  plane shown in Figure 14. Combined with our measurement of  $H_0$  we find  $w = -1.12 \pm 0.12$ , a value consistent with a cosmological constant ( $\Lambda$ ). This result is similar in value and precision to those found from the combination of baryon acoustic oscillations (BAO) and high-redshift SNe Ia (Wood-Vasey et al. 2007; Astier et al. 2006). The important difference from the prior measurements is that it is independent of the systematic uncertainties associated with the use of high-redshift SNe Ia. Since such measurements are now dominated by

---

<sup>9</sup><http://lambda.gsfc.nasa.gov/> .

their systematic errors (Wood-Vasey et al. 2007, Kessler et al. 2009, Hicken et al. 2009, Kowalski et al. 2008), independent measurements are a route to progress. For comparison, the combination of the WMAP and BAO data alone gives  $w = -1.15 \pm 0.22$  and that from WMAP and the Freedman et al. (2001) measurement of  $H_0$  yields  $w = -1.01 \pm 0.23$ .

The  $H_0$ +WMAP measurement of  $w$  is quite insensitive to the effect of  $w$  on the determination of  $a_v$  because the mean redshift of the Hubble flow sample is only  $z = 0.04$ . Specifically, the change in  $H_0$  for a change in  $w$  of 0.1 (evaluated at  $z = 0.04$ ) is only 0.2%, far less than the total 4.8% uncertainty in  $H_0$  and justifying our use of a kinematic expansion to determine  $a_v$ . The very mild degeneracy between  $a_v$  and  $w$  is shown (as a tilt) in Figure 14.

However, fitting a cosmological model with the assumption of a *constant* equation of state (EOS) is itself limiting to the investigation of dark energy. It obscures our ability to detect evolution of  $w$ , an important test of the presence of a cosmological constant. An alternative approach is to use a variant of principal-component analysis (Huterer & Starkman 2003; Huterer & Cooray 2005) to extract discrete, decorrelated estimates of  $w(z)$ , binned in redshift. This method was used by Riess et al. (2007) and Sullivan et al. (2007) to constrain multiple independent measures of  $w(z)$ . With the improved constraint on  $H_0$ , we can use this approach to determine the effect on the constraints on the components of  $w(z)$ . In the following we employ the implementation of the component analysis from Sarkar et al. (2008) using  $N + 3$  free parameters in the MCMC corresponding to  $H_0$ ,  $\Omega_m$ ,  $\Omega_K$ , and the  $N$  independent estimates of  $w$ .

### 5.1. Current Data

We first examine how the errors on  $w(z)$  improve from using the improved constraint on  $H_0$ . For this we use the Davis et al. (2007) compilation of 192 SNe, 2 BAO estimates from Percival et al. (2007), and the WMAP 5-year constraint (Komatsu et al. 2008) on the distance to the last-scattering surface ( $R_{\text{CMB}}$ ) in the  $H_0$ -independent form. We also use the WMAP 5-year constraint on  $\Omega_m h^2$  (Komatsu et al. 2008) and allow curvature to be free. We use the publicly available *wzBinned*<sup>10</sup> code and analyze the data using an MCMC likelihood approach to estimate  $w(z)$  in each redshift bin. We take a total of 3 bins between  $z = 0$  and  $z = 1.8$  (see Table 8 for the redshift ranges) and assume that dark energy at  $z > 2$  was subdominant by fixing  $w$  to a constant value of  $-1$  from that redshift to the last-scattering surface ( $z = 1089$ ).

We analyze the data using the value of  $H_0$  from both *HST* Cepheids (Freedman et al. 2001) and the present work. Our results are summarized in Table 8. Using the new constraints on the Hubble constant we get a significant improvement on the  $1\sigma$  errors of the EOS parameters. The improvement in the inverse product of the uncertainties in  $w(z)$ , widely referred to as a dark energy "figure of merit", improves by a factor of 3 due to the increased precision in  $H_0$ , a

---

<sup>10</sup><http://dsarkar.org/code.html> .

result of the degeneracy between  $w$  and  $H_0$ . The data remain consistent with  $\Lambda$  within  $1\sigma$  with  $[w_1, w_2, w_3] = [-0.947_{-0.116}^{+0.116}, -0.877_{-0.166}^{+0.140}, -0.687_{-0.613}^{+0.289}]$  for the ranges  $z = [0-0.2], [0.2-0.5], [0.5-1.8]$ , respectively. The data continue to indicate the presence of a dark energy component (i.e.,  $w < 0$ ) when it was a sub-dominant part of the Universe, in agreement with Riess et al. (2007) (see also Kowalski et al. 2008).

## 5.2. Future Surveys

We now consider the constraints on  $w(z)$  from future surveys in three different scenarios under frequent consideration:

Case (1): An aggressive set of 17 BAO distance measurements. This includes 2 BAO estimates (as before) at  $z = 0.2$  and  $z = 0.35$ , with 6% and 4.7% uncertainties, respectively (Percival et al. 2007); 5 BAO constraints at  $z = [0.6, 0.8, 1.0, 1.2, 3.0]$  from SDSS III and HETDEX with respective precisions of  $[1.9, 1.5, 1.0, 0.9, 0.6]\%$  (Seo & Eisenstein 2003, scenario V5N5); and 10 BAO estimates from a space mission with precisions of  $[0.36, 0.33, 0.34, 0.33, 0.31, 0.33, 0.32, 0.35, 0.37, 0.37]\%$  from  $z = 1.05$  to  $1.95$  in steps of  $0.05$ .

Case (2): An aggressive SN Ia data set of 2300 SNe with 300 SNe uniformly distributed out to  $z = 0.1$ , as expected from ground-based low-redshift samples, and an additional 2000 SNe uniformly distributed in the range  $0.1 < z < 1.7$ , as expected from future space mission (Kim et al. 2004). We bin the Hubble diagram into 32 redshift bins (corresponding to a width of the relevant redshift bin of  $\Delta z = 0.05$ ). The error in the distance modulus for each SN bin is given by  $\sigma_m = ((\sigma_{\text{int}}/N_{\text{bin}}^{1/2})^2 + \delta m^2)^{1/2}$ , where  $\sigma_{\text{int}} = 0.1$  mag is the intrinsic error for each SN,  $N_{\text{bin}}$  is the number of SNe in the redshift bin, and  $\delta m$  is the irreducible systematic error. We take the systematic error to have the form  $\delta m = 0.02(0.1/\Delta z)^{1/2}(1.7/z_{\text{max}})(1+z)/2.7$ , where  $z_{\text{max}}$  is the redshift of the most distant SNe. This is equivalent to the form in Linder & Huterer (2003). In generating the SN catalog, we do not include the effect of gravitational lensing, as it is expected to be small (Sarkar et al. 2008) and should not affect our results much.

Case (3): A combination of the above: 2300 SNe and 17 BAO estimates.

For each of the above-mentioned scenarios, we also use the WMAP 5-year constraint on  $R_{\text{CMB}}$  (Komatsu et al. 2008). Since we are considering future surveys, we marginalize over  $\Omega_m$  prior obtained from the Planck prior on  $\Omega_m h^2$  and different priors on  $H_0$  (see Table 9 for details). As before, we allow the curvature to be free. In this case, we take a total of 6 bins between  $z = 0$  and  $z = 2$  (see Table 9 for the redshift ranges) and fix  $w(2 < z < 1089) = -1$ . The sixth bin (extending from  $z = 1.2$  to  $z = 2.0$ ) is suppressed as it is not well constrained.

Table 9 and Figure 15 summarize our results. A significant improvement of the 68% error in the decorrelated binned estimates of  $w$  is apparent as we make use of better constraints on the Hubble constant.

Further improvement in the measurement of  $H_0$  should allow for the measurement of a fourth independent parameter of the EOS to an accuracy better than 10%, even without making use of any BAO estimate. A combination of next-generation surveys will most likely be able to measure five independent parameters of the EOS to better than 10% accuracy.

An alternative use of a precise measurement of  $H_0$  is as an “end-to-end” test of the best constraints on the cosmological model from all other data. As shown in Table 1, the combination of measurements from WMAP, BAO, and high-redshift SNe Ia, together with the assumption of a constant value for  $w$ , predict  $H_0$  to greater precision than measured here. This prediction is in good agreement with our measurement, but belies tension between the predictions of  $H_0$  from BAO and high-redshift SNe Ia. Either of these combined with WMAP results in a  $3\sigma$  difference in their prediction of  $H_0$ . Although our present measurement lies between these two combinations, it is closer to BAO and inconsistent with WMAP and high-redshift SNe Ia at the  $2.8\sigma$  confidence level. Improvements in all datasets should reveal whether this tension results from systematic error or is indicative of the need for a more complex description of dark energy.

## 6. Discussion

Ever more precise measurements of the Hubble constant can contribute to the determination of the even more elusive nature of dark energy. The Planck CMB mission is expected to measure  $\Omega_M H_0^2$  to 1%. A complementary goal would be to reach the same for  $H_0$ . We show in Figure 15 that a measurement of  $H_0$  approaching 1% would be competitive with “next generation” measurements of BAO and high-redshift SNe Ia (Kolb et al. 2006) for constraining the evolution of  $w$ , and could supplant either tool should they encounter insurmountable systematic errors before reaching their goals. Attempts to explain accelerated expansion without dark energy by an unexpected failure of the cosmological principle also benefit from improved measurements of  $H_0$ . For example, an approach by (Wiltshire 2007) in this vein predicts  $H_0 = 62 \pm 2$  which is already inconsistent with the present measurement at the  $3\sigma$  confidence level.

How realistic is a measurement of  $H_0$  to 1%? In most respects, the measurement of  $H_0$  to 1% is no more ambitious than the plans to push high-redshift SN Ia measurements to their next level of precision. Indeed, the dominant sources of systematic uncertainty in measuring distant SNe Ia do not pertain to  $H_0$  as they result from large redshifts: cross-filter, cross-detector flux calibration,  $K$ -corrections, and evolution of SNe Ia and dust over large changes in redshift (Wood-Vasey et al. 2007).

Following Table 7, we consider the two biggest challenges to a 1% measurement of  $H_0$ : the precision of the distance measurement of the anchor and the size of the calibrator sample of SNe Ia. The other terms are near or below 1% and can be reduced with the collection of more data.

Further improvements in the distance measurement to NGC 4258 requires understanding and modeling additional complexity in its inner disk, including eccentricity and the presence of spiral

structure (Humphreys et al. 2008, 2009). We expect progress with future work, though 1% or better would be challenging. With the present route it may be possible to measure  $H_0$  to 2% or 3%.

More maser hosts of comparable quality could further reduce the uncertainty in the anchor through averaging. The Maser Cosmology Project (MCP; Braatz et al. 2008) is a large project at NRAO with the goal of measuring 10 more hosts in the next 5 years (Greenhill et al. 2009). Of the 112 extragalactic maser galaxies now known, 30% show the required high-velocity features on their limbs and 10% are disks and are good candidates for distance measurements. Two of these, UGC 3789 and NGC 6323, have already yielded initial distance estimates with 15% uncertainty and which, combined with their redshifts, are consistent with the value of  $H_0$  inferred here (Braatz 2008, private comm.; Lo 2008, private comm.). Reaching 1% will require the 10 new MCP maser hosts to each be measured to the 3% uncertainty of NGC 4258 (Greenhill et al. 2009), or some other combination of number of systems and individual precision. Considering that the majority of maser hosts have been found in the last 5 years, there is reason for optimism in the future. If such a sample of maser hosts is collected, it would then be necessary to correct their recession velocities for peculiar and coherent flows (Hui et al. 2006) to a mean of 1% or observe their Cepheids to tie their distance scale to the 0.5% calibration of the Hubble flow from SNe Ia.

Another promising route is offered by GAIA which should collect a few hundred high-precision parallax measurements for long-period Cepheids in the Galaxy. The resulting  $P$ - $L$  relations would be more than sufficient to support a 1% measurement of  $H_0$ . However, the comparison of bright Galactic Cepheids and faint ones in SN hosts raises the challenge of measuring fluxes over a range of 20 mag to better than 1% precision. Though formidable, this appears easier than the challenge facing future high-redshift SN Ia studies because the Cepheid measurements may all be obtained at the same wavelengths. Accounting for the difference in crowding between Galactic and extragalactic Cepheids is also a concern.

The size of the sample of reliable SNe Ia close enough to resolve Cepheids in their hosts, those within  $\sim 30$  Mpc, presently limits the determination of their mean fiducial luminosity to 2.5%. At least 30 SNe Ia are needed in this sample and at a rate of  $\sim 1$  new object appearing every 3 yr we cannot wait on Nature. A factor of 2 increase in distance (factor of 8 in volume), and hence 1.5 mag in the range of resolving Cepheids, is needed. Ultra-long-period Cepheids with  $80 < P < 180$  d (Bird et al. 2008) and  $M_V = -7$  mag are  $\sim 2$  mag brighter than the typical,  $P = 30$  d Cepheids observed in SN hosts. Though these Cepheids appear to obey different  $P$ - $L$  relations than their shorter-period brethren and are rare, their use when intercompared between galaxies is promising (Bird et al. 2008, Riess et al. 2009). JWST is expected to routinely resolve Cepheids at  $\sim 50$  Mpc and could be enlisted to help measure  $H_0$  to 1%.

## 7. Summary and Conclusions

(1) We have observed 240 long-period Cepheids in 6 SN Ia hosts and NGC 4258 using NICMOS in *F160W*.

(2) Unprecedented homogeneity in the periods and metallicity in the use of these Cepheids along the distance ladder greatly reduces systematic uncertainties

(3) Use of the same telescope, instrument, and filters for all Cepheids also reduces the systematic uncertainty related to flux calibration.

(4) Our primary analysis gives  $H_0 = 74.2 \pm 3.6 \text{ km s}^{-1} \text{ Mpc}^{-1}$ .

(5) Alternative analyses using different extinction laws and extinction distributions yield consistent results.

**We are grateful to William Januszewski, William Workman, Neil Reid, Howard Bond, Louis Bergeron, Rodger Doxsey, Craig Wheeler, Malcolm Hicken, Robert Kirshner, Peter Challis, Elizabeth Humphreys, Lincoln Greenhill, and Ken Sembach for their help in realizing this measurement.**

Financial support for this work was provided by NASA through programs GO-9352, GO-9728, GO-10189, GO-10339, and GO-10802 from the Space Telescope Science Institute, which is operated by AURA, Inc., under NASA contract NAS 5-26555. A.V.F.'s supernova group at U.C. Berkeley is also supported by NSF grant AST-0607485 and by the TABASGO Foundation.

## Figure Captions

Figure 1: Optical images of SNe Ia near peak (see Figures 2 to 7 for orientations and scales). These images show the objects used to calibrate the SN Ia fiducial luminosity. The images were obtained with CCDs. The exception is SN 1981B which was observed photoelectrically and with the Texas Grival electrographic camera (image shown here) which has better sensitivity and linearity than photographic plates.

Figure 2: *HST* ACS *F555W* image of NGC 3370. The positions of Cepheids with periods in the range  $P > 60$  d,  $30 < P < 60$  d and  $10 < P < 30$  d are indicated by red, blue, and green circles, respectively. A yellow circle indicates the position of the host’s SN Ia. The orientation is indicated by the compass rose whose vectors have lengths of  $15''$ . The fields of view for the NIC2 follow-up fields in Table 2 are indicated.

Figure 3. As Figure 2 for NGC 1309.

Figure 4: As Figure 2 for NGC 3021.

Figure 5: As Figure 2 for NGC 4639

Figure 6: As Figure 2 for NGC 4536, image from *HST* WFPC2.

Figure 7: As Figure 2 for NGC 3982

Figure 8: Example of scene modeling for the arcsec surrounding each Cepheid in one NIC2 field, NGC3370-GREEN. For each Cepheid, the stamp on the left shows the region around the Cepheid, the middle stamp shows the model of the stellar sources, and the right stamp is the residual of the image minus the model. The position of the Cepheid as determined from the optical data is indicated by the circle.

Figure 9: Example of the artificial stars tests in the region around a Cepheid in the field NGC3021-GREEN with  $P = 82.0$  days. A thousand artificial stars of the brightness of the Cepheid (as determined from its period) are randomly added to the image. The magnitudes of the artificial stars are measured at their known positions (in the same way as the Cepheids). The difference between the input and measured star magnitudes (i.e., the bias) is shown as a function of the displacement between the injected position and the centroid of the star found nearest this position. The photometric bias (brighter) increases with the displacement, a direct consequence of blending. For displacements beyond a pixel, the recovered star is no longer the same as the one injected and the relation between bias and displacement dissipates. Averages and dispersions in bins of the displacement are indicated by the filled dots. For an individual Cepheid, the displacement between the NICMOS and optical position is used to predict and correct for the bias as shown in the vertical dotted line. The uncertainty is derived from the dispersion of the artificial stars.

Figure 10: Example NIC2 fields for the anchor galaxy, NGC 4258 (NIC-POS3, right), and a SN field, NGC3370-GREEN (left). The Cepheid positions are indicated. The artificial star tests show that the mean photometric bias in the Cepheid magnitudes due to blending is very similar

for these fields (0.14 mag for the anchor and 0.16 mag for the SN host), not surprising from the apparent similarity of their stellar density. Thus, the *difference* in Cepheid magnitudes in these hosts, the quantity used to construct the distance ladder, is quite insensitive to blending.

Figure 11: Near-infrared Cepheid period-luminosity relations. For the 6 SN Ia hosts and the distance-scale anchor, NGC 4258, the Cepheid magnitudes are from the same instrument and filter combination, NIC2 *F160W*. This uniformity allows for a significant reduction in systematic error when utilizing the difference in these relations along the distance ladder. The measured metallicity for all the Cepheids is solar-like ( $12+\log [\text{O}/\text{H}] \sim 8.9$ ). A single slope has been fit to the relations and is shown as the solid line. 10% of the objects were outliers from the relations (open diamonds) and are flagged as such for the subsequent analysis. Filled points with asterisks indicate Cepheids whose periods are shorter than the incompleteness limit identified from their optical detection. The lower right panel shows the near-IR *P-L* relation derived from 10 Milky Way Cepheids with precise, individual parallax measurements from Benedict et al. (2007).

Figure 12: The magnitude-redshift relation of nearby ( $z < 0.1$ ) SNe Ia. The term  $m_V^0$  is the peak apparent magnitude in *V* corrected for extinction and to the fiducial luminosity using a light-curve fitter. The intercept of the linear relation defines the term  $a_v = \log cz - 0.2m_V^0$  used for the determination of  $H_0$ . SNe Ia with redshifts in the range  $z > 0.01$  or  $z > 0.0233$  are used in the analysis.

Figure 13: Relative distances from Cepheids and SNe Ia. The x-axis (bottom) shows the peak apparent visual magnitude of each SN Ia (red points) corrected for reddening and to the fiducial brightness (using the luminosity-light curve shape relations),  $m_V^0$ . The upper x-axis includes the intercept of the  $m_V^0$ - $\log cz$  relation for SNe Ia,  $a_v$  to provide SN Ia distance measures,  $m_V^0 + 5a_v$ , which are independent of the light curve shape relations. The y-axis (right), shows the relative distances between the hosts determined from the Cepheid *VIH* Wesenheit relations. The left y-axis shows the same with the addition of the independent geometric distance to NGC 4258 (blue point) based on its circumnuclear masers. The contribution of the nearby SNe Ia and Cepheid data to  $H_0$  can be expressed as a determination of  $m_{V,4258}^0$ , the theoretical mean of 6 fiducial SNe Ia in NGC 4258.

Figure 14: Confidence regions in the plane of  $H_0$  and the equation of state of dark energy,  $w$ . The localization of the 3rd acoustic peak in the WMAP 5 year data (Komatsu et al. 2008) produces a confidence region which is narrow but highly degenerate in this space. The improved measurement of  $H_0$ ,  $74.2 \pm 3.6 \text{ km s}^{-1} \text{ Mpc}^{-1}$ , from the SHOES program is complementary to the WMAP constraint resulting in a determination of  $w = -1.12 \pm 0.12$  for a constant equation of state. This result is comparable in precision to determinations of  $w$  from baryon acoustic oscillations and high-redshift SNe Ia, but is independent of both. The inner regions are 68% confidence and the outer regions are 95% confidence. The modest tilt of the SHOES measurement of 0.2% in  $H_0$  for a change in  $w=0.1$  results from the mild dependence of  $a_v$  on  $w$  at the mean  $z = 0.04$ . The measurement of  $H_0$  is made at  $j_0 = 1$  (i.e.,  $w = -1$ ).

Figure 15: Projected constraints on 5 principal components of  $w(z)$  as a function of the future precision of  $H_0$ . Three future scenarios are considered: an aggressive BAO experiment (black), an aggressive high- $z$  SN Ia experiment (red), or both (blue) along with a Planck-based prior on  $\Omega_m h^2$ . Panels 1 to 5 show the expected constraints in different redshift ranges. Panel 6 shows a figure of merit, the inverse product of the uncertainties of the 5 components. As seen, a  $\sim 1\%$  measurement of  $H_0$  can compensate for either BAO or high- $z$  SNe Ia being limited by systematic errors or can aid their joint use.

Table 4—Continued

Field	$\alpha$ (J2000)	$\delta$ (J2000)	Id	P (days)	$V - I$ (mag)	$F160W$ (mag)	$\sigma$ (mag)	Offset (pix)	Bias (mag)	Phase (mag)	[O/H]	Flag <sup>a</sup>	Src*
NIC-POS7	184.85593	47.16107	104251	33.29	1.04	22.56	0.18	0.03	0.01	-0.13	8.64		lm
NIC-POS8	184.79990	47.20616	220789	21.29	1.04	23.31	0.19	0.35	0.04	0.16	8.77		lm
NIC-POS8	184.79992	47.20734	220887	31.29	1.26	22.70	0.18	0.15	0.00	-0.14	8.77		lm
NIC-POS8	184.80002	47.20401	220576	101.9	1.92	20.22	0.25	0.11	0.01	-0.02	8.76		lm
OUT-NIC-02	184.81866	47.19866	34729	14.92	1.12	23.44	0.23	0.22	0.07	-0.01	8.75		lm
OUT-NIC-04	184.83594	47.22012	28606	53.88	1.03	21.76	0.18	0.25	0.03	0.09	8.76		lm
OUT-NIC-05	184.83415	47.19030	21109	8.503	0.86	23.98	0.27	8.81	0.34	0.04	8.72		lm
OUT-NIC-06	184.83914	47.17078	12705	9.942	0.84	24.23	0.25	0.31	0.07	-0.08	8.67		lm
OUT-NIC-06	184.83644	47.17427	14709	10.97	0.84	23.68	0.22	0.42	-0.00	0.10	8.68		lm
OUT-NIC-06	184.83530	47.17378	15276	16.43	0.87	23.62	0.21	0.62	0.03	-0.07	8.68		lm
OUT-NIC-07	184.83867	47.19483	19312	13.55	0.82	23.32	0.21	0.52	0.07	-0.08	8.72		lm
OUT-NIC-08	184.85030	47.19245	11990	8.024	0.65	23.78	0.22	0.34	0.09	0.10	8.71		lm
OUT-NIC-09	184.85468	47.16904	5713	31.74	0.96	22.41	0.18	0.14	0.02	-0.15	8.66		lm
OUT-NIC-10	184.85857	47.20057	9786	8.920	0.72	23.85	0.24	0.28	0.14	-0.05	8.70		lm
OUT-NIC-13	184.83969	47.18170	14656	8.779	0.80	24.23	0.35	1.52	0.06	0.03	8.70		lm

\* Source of Optical Cepheid parameters. lm=L.M. from Riess et al. 2009 and Macri et al. 2009, psl=P.B.S. from Gibson & Stetson 2000

<sup>a</sup> Cepheid Rejection Flag. <P indicates that the period is shorter than the optical completeness from Riess et al. 2009, rej is  $\sigma$  clipped

Table 5: Distance Parameters

Host	SN Ia	filters	$m_{v,i}^0 + 5a_v$	$\sigma^a$	$\mu_{0,i} - \mu_{0,4258}$
NGC 4536	SN 1981B	UBVR	15.156	0.145	1.145 (0.0845)
NGC 4639	SN 1990N	UBVRI	16.059	0.111	2.185 (0.0963)
NGC 3982	SN 1998aq	UBVRI	15.976	0.091	2.473 (0.101)
NGC 3370	SN 1994ae	UBVRI	16.578	0.102	2.831 (0.0771)
NGC 3021	SN 1995al	UBVRI	16.726	0.113	2.914 (0.101)
NGC 1309	SN 2002fk	BVRI	16.806	0.103	3.261 (0.0861)
Weighted Mean	—	—	—	0.0448	— (0.0367)

<sup>a</sup> For MLCS2k2, 0.08 mag added in quadrature to fitting error.

Table 6. Fits for  $H_0$

$\chi_{dof}^2$	#	$H_0$	$\sigma_{fit}$	$a_v$	$M_V^0$	$\delta M/\delta[\text{O}/\text{H}]$	b	$z_{min}$	Fit	Scale	PLW	C $R_V$	SNe	SN $R_V$
0.85	209	74.16(3.41)	2.56	0.698	-19.13	-0.23(0.17)	-3.14(0.10)	0.023	37	4258	$H_{V,I}$	3.1	UBVRI	2.5
0.84	209	73.97(3.44)	2.60	0.702	-19.16	-0.22(0.17)	-3.15(0.10)	0.023	20	4258	$H_{V,I}$	3.1	UBVRI	3.1
0.83	209	75.12(3.43)	2.56	0.702	-19.13	-0.22(0.17)	-3.12(0.10)	0.010	37	4258	$H_{V,I}$	2.5	UBVRI	2.5
0.82	209	75.10(3.46)	2.61	0.707	-19.15	-0.21(0.17)	-3.12(0.10)	0.010	20	4258	$H_{V,I}$	2.5	UBVRI	3.1
0.85	209	73.27(3.30)	2.43	0.698	-19.16	—	-3.17(0.10)	0.023	37	4258	$H_{V,I}$	3.1	UBVRI	2.5
1.41	240	77.24(4.05)	3.30	0.698	-19.05	-0.72(0.20)	-3.10(0.13)	0.023	37	4258	$H_{V,I}$	3.1	UBVRI	2.5
0.86	198	74.62(3.49)	2.64	0.698	-19.12	-0.31(0.18)	-3.13(0.11)	0.023	37	4258	$H_{V,I}$	3.1	UBVRI	2.5
0.85	209	73.19(3.45)	2.63	0.701	-19.18	-0.24(0.17)	-3.14(0.10)	0.023	61	4258	$H_{V,I}$	3.1	BVRI	2.5
0.81	209	74.66(3.37)	2.49	0.692	-19.09	-0.22(0.17)	-3.09(0.10)	0.023	28	4258	$H_{V,I}$	2.0	UBVRI	2.0
0.84	209	73.51(3.30)	2.35	—	—	-0.23(0.17)	-3.14(0.10)	0.023	42	4258	$H_{V,I}$	3.1	UBVRI	—
0.82	209	73.79(3.29)	2.33	—	—	-0.23(0.17)	-3.12(0.10)	0.023	42	4258	$H_{V,I}$	2.5	UBVRI	—
0.84	209	74.84(3.37)	2.40	—	—	-0.23(0.17)	-3.15(0.10)	0.010	42	4258	$H_{V,I}$	3.1	UBVRI	—
0.79	209	75.64(3.41)	2.52	0.698	-19.09	-0.19(0.17)	-3.01(0.10)	0.023	37	4258	$H$	3.1	UBVRI	2.5
0.79	209	74.88(3.31)	2.39	0.698	-19.11	—	-3.03(0.10)	0.023	37	4258	$H$	3.1	UBVRI	2.5
0.83	209	73.20(3.47)	2.65	0.690	-19.13	-0.19(0.17)	-3.15(0.10)	0.023	26	4258	$H_{V,I}$	3.1	UBVRI	3.1
0.84	209	74.05(3.50)	2.60	0.699	-19.15	-0.22(0.17)	-3.15(0.10)	0.023	27	4258	$H_{V,I}$	3.1	UBVRI	3.1
0.85	209	74.10(3.38)	2.53	0.692	-19.11	-0.24(0.17)	-3.14(0.10)	0.023	28	4258	$H_{V,I}$	3.1	UBVRI	2.0
0.85	209	74.11(3.36)	2.50	0.687	-19.08	-0.25(0.17)	-3.14(0.10)	0.023	29	4258	$H_{V,I}$	3.1	UBVRI	1.5
0.84	219	74.91(4.13)	4.11	0.698	-19.11	-0.21(0.17)	-3.20(0.09)	0.023	37	MW	$H_{V,I}$	3.1	UBVRI	2.5
0.85	219	73.68(3.93)	3.91	0.698	-19.15	—	-3.22(0.09)	0.023	37	MW	$H_{V,I}$	3.1	UBVRI	2.5
0.84	219	74.68(4.15)	4.13	0.702	-19.14	-0.20(0.17)	-3.21(0.09)	0.023	20	MW	$H_{V,I}$	3.1	UBVRI	3.1
0.78	219	74.56(3.97)	3.95	0.698	-19.12	-0.18(0.17)	-3.06(0.09)	0.023	37	MW	$H$	2.5	UBVRI	2.5
1.01	262	73.27(4.57)	2.71	0.698	-19.16	—	-3.17(0.04)	0.023	37	LMC	$H_{V,I}$	2.5	UBVRI	2.5

Table 7: Error Budget for  $H_0$  for Cepheid and SN Ia Distance Ladders

Term	Description	Previous	Here
$\sigma_{\text{anchor}}$	Anchor distance	5%	3%
$\sigma_{\text{anchor-PL}}$	Mean of $P-L$ in anchor	2.5%	1.5%
$\sigma_{\text{host-PL}}/\sqrt{n}$	Mean of $P-L$ values in SN hosts	1.5%	1.5%
$\sigma_{\text{SN}}/\sqrt{n}$	Mean of SN Ia calibrators	2.5%	2.5%
$\sigma_{\text{mag-z}}$	SN Ia $m-z$ relation	1%	0.5%
$R\sigma_{\lambda,1,2}$	Cepheid reddening, zeropoints, anchor-to-hosts	4.5%	0.3%
$\sigma_Z$	Cepheid metallicity, anchor-to-hosts	3%	0.8%
$\sigma_{\text{PL}}$	$P-L$ slope, $\Delta \log P$ , anchor-to-hosts	4%	0.5%
$\sigma_{\text{WFPC2}}$	WFPC2 CTE, long-short	3%	0%
Total, $\sigma_{H_0}$		10%	4.8%

Table 8: Decorrelated Estimates of  $w$  from Available Datasets (68% Uncertainty)

Dataset used	Prior on	$w_1$	$w_2$	$w_3$
	$H_0$	$z=[0-0.2]$	$z=[0.2-0.5]$	$z=[0.5-1.8]$
192 SNe + 2 BAO	$72 \pm 8.0$	$-0.976^{+0.142}_{-0.162}$	$-0.944^{+0.230}_{-0.235}$	$-0.471^{+0.327}_{-1.515}$
	$74 \pm 3.5$	$-0.940^{+0.102}_{-0.139}$	$-0.948^{+0.175}_{-0.160}$	$-0.692^{+0.301}_{-0.759}$

Table 9: 68% Error in the Decorrelated Binned Estimates of  $w$  from Upcoming Surveys

Mocks used	$H_0$ 74±	$\Delta w_1$ z=[0-0.07]	$\Delta w_2$ z=[0.07-0.15]	$\Delta w_3$ z=[0.15-0.30]	$\Delta w_4$ z=[0.3-0.6]	$\Delta w_5$ z=[0.6-1.2]	FoM ( $\times 10^4$ )
17 BAO	8.0	0.549	0.462	0.323	0.202	0.158	0.038
	6.0	0.389	0.374	0.255	0.196	0.166	0.083
	4.0	0.342	0.340	0.238	0.174	0.150	0.138
	3.5	0.331	0.329	0.224	0.163	0.143	0.176
	2.0	0.203	0.203	0.144	0.118	0.131	1.090
	1.0	0.130	0.134	0.096	0.081	0.093	7.938
2300 SNe	8.0	0.128	0.137	0.162	0.308	7.999	0.014
	6.0	0.127	0.132	0.156	0.294	8.799	0.015
	4.0	0.105	0.098	0.105	0.193	1.622	0.296
	3.5	0.098	0.085	0.088	0.145	1.334	0.705
	2.0	0.091	0.070	0.064	0.083	0.291	10.16
	1.0	0.078	0.052	0.043	0.048	0.124	96.33
2300 SNe + 17 BAO	8.0	0.064	0.054	0.045	0.048	0.104	129
	6.0	0.063	0.051	0.042	0.045	0.099	166
	4.0	0.063	0.049	0.041	0.043	0.097	189
	3.5	0.062	0.049	0.041	0.043	0.092	203
	2.0	0.061	0.047	0.038	0.039	0.086	274
	1.0	0.057	0.043	0.034	0.034	0.065	543

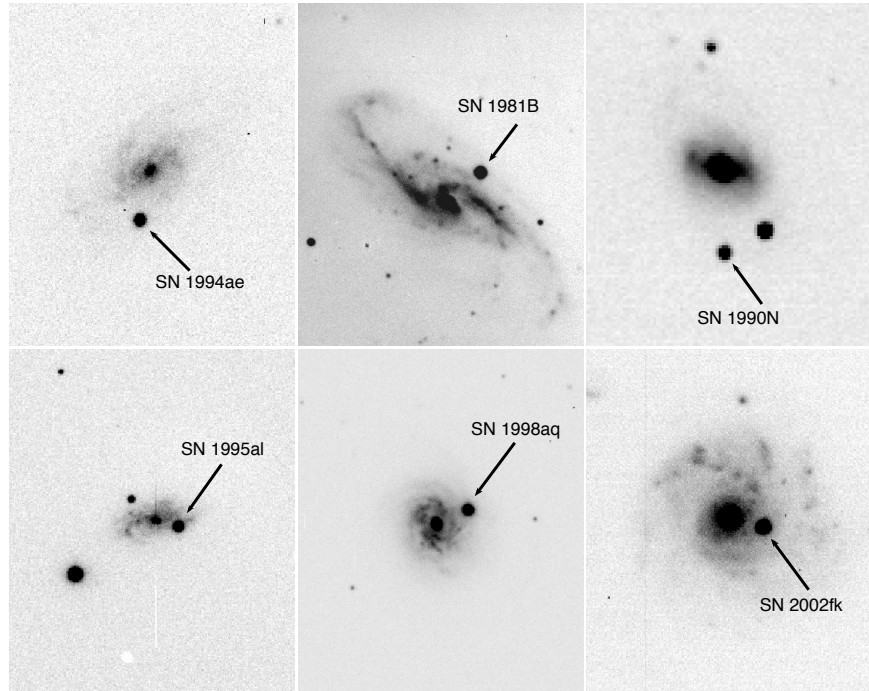


Fig. 1.—

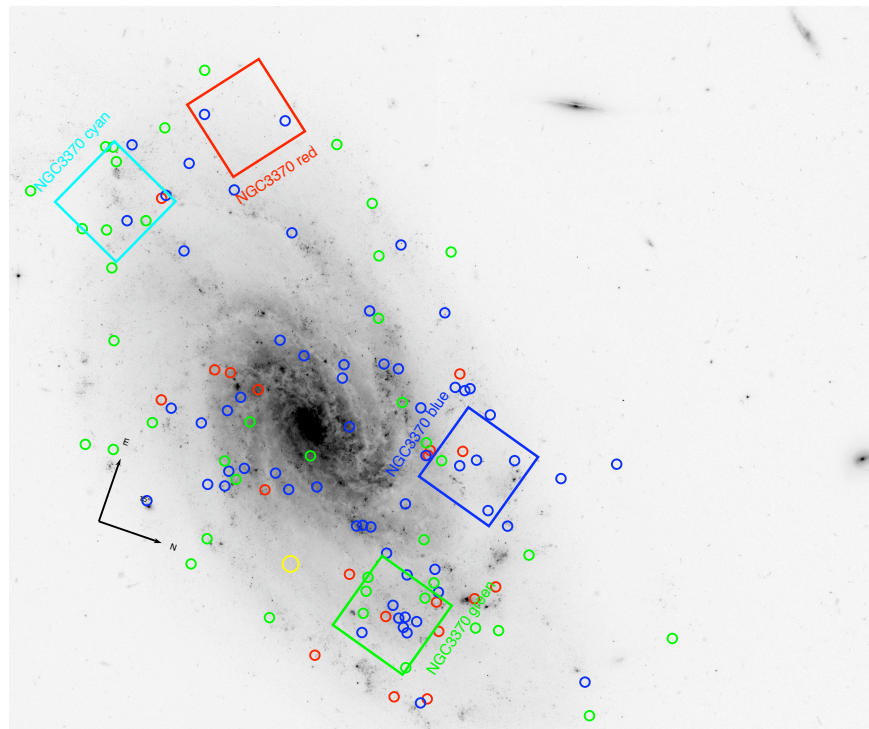


Fig. 2.—

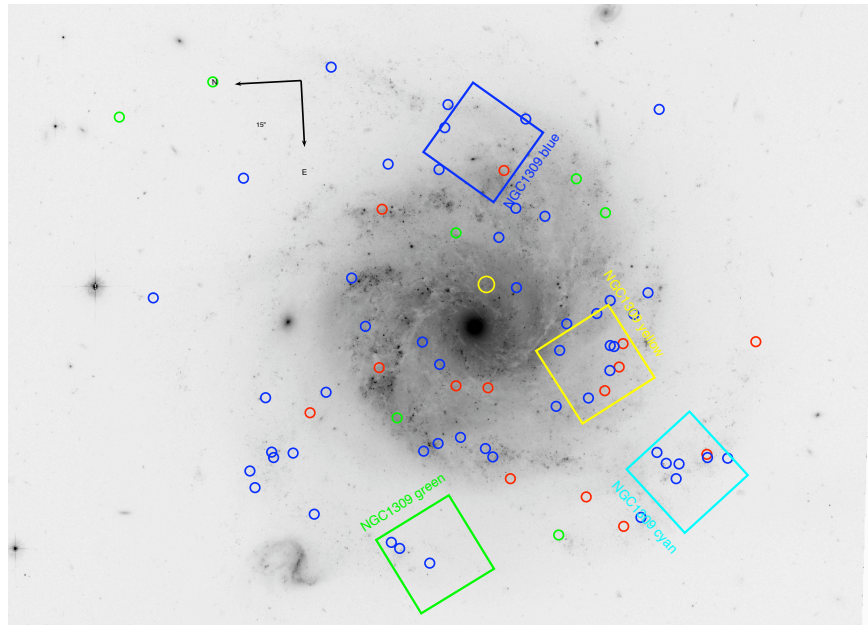


Fig. 3.—

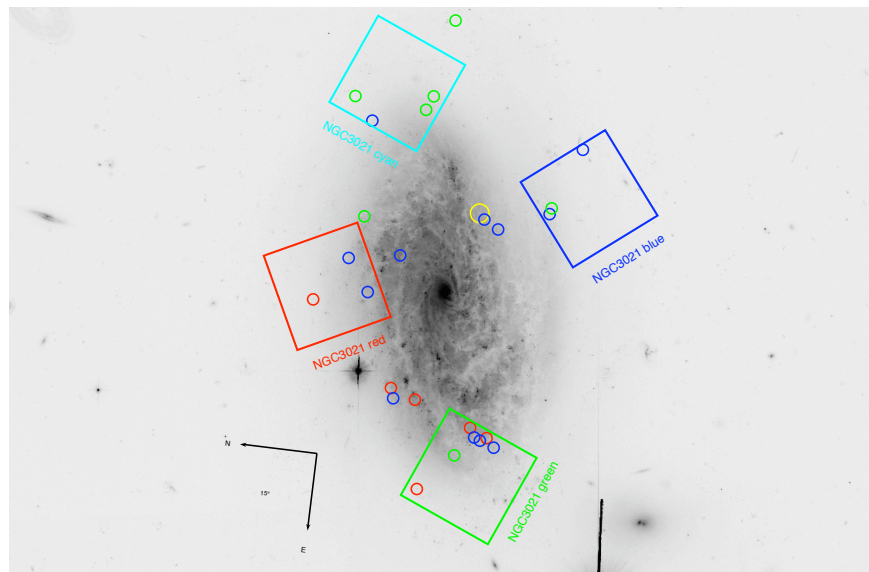


Fig. 4.—

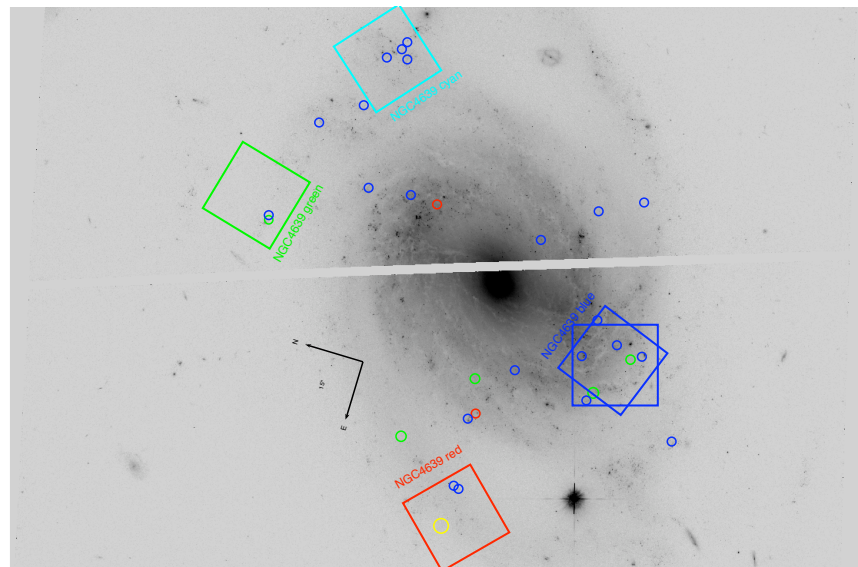


Fig. 5.—

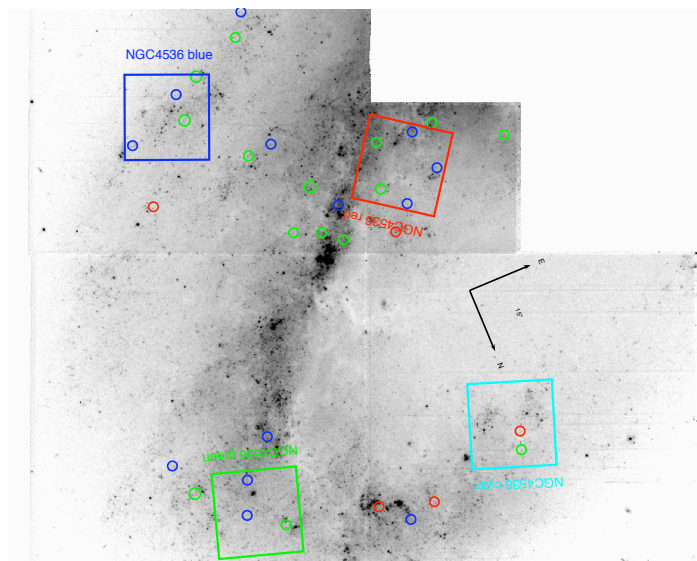


Fig. 6.—

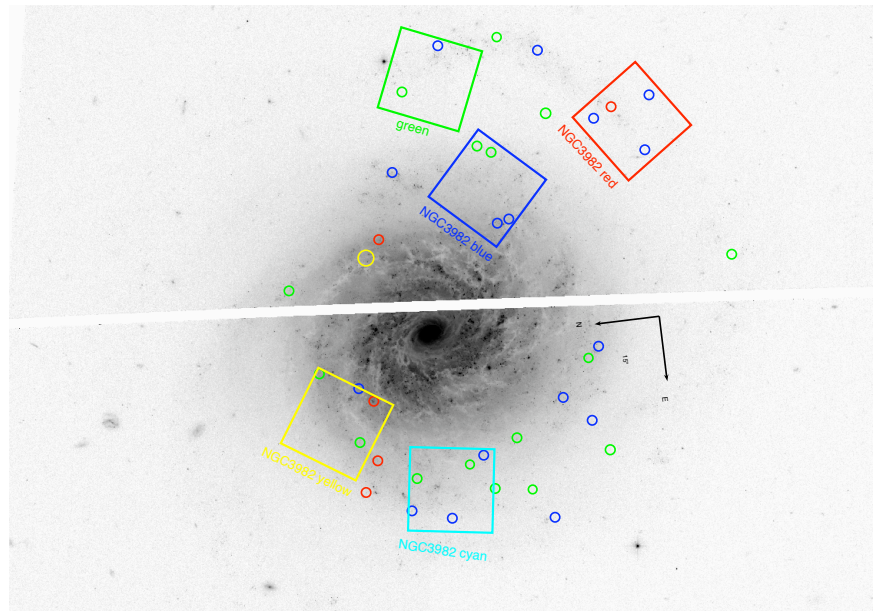


Fig. 7.—

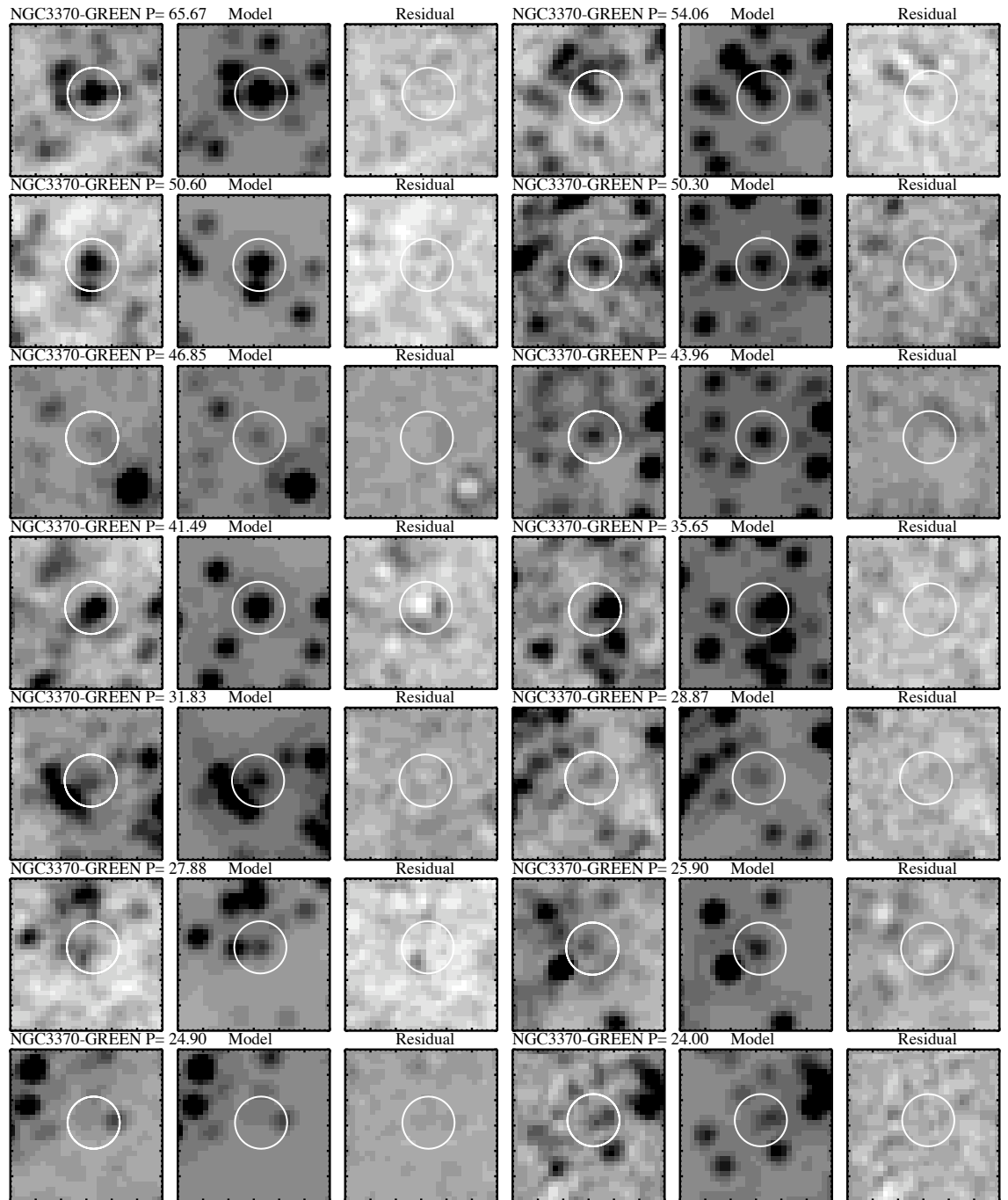


Fig. 8.—

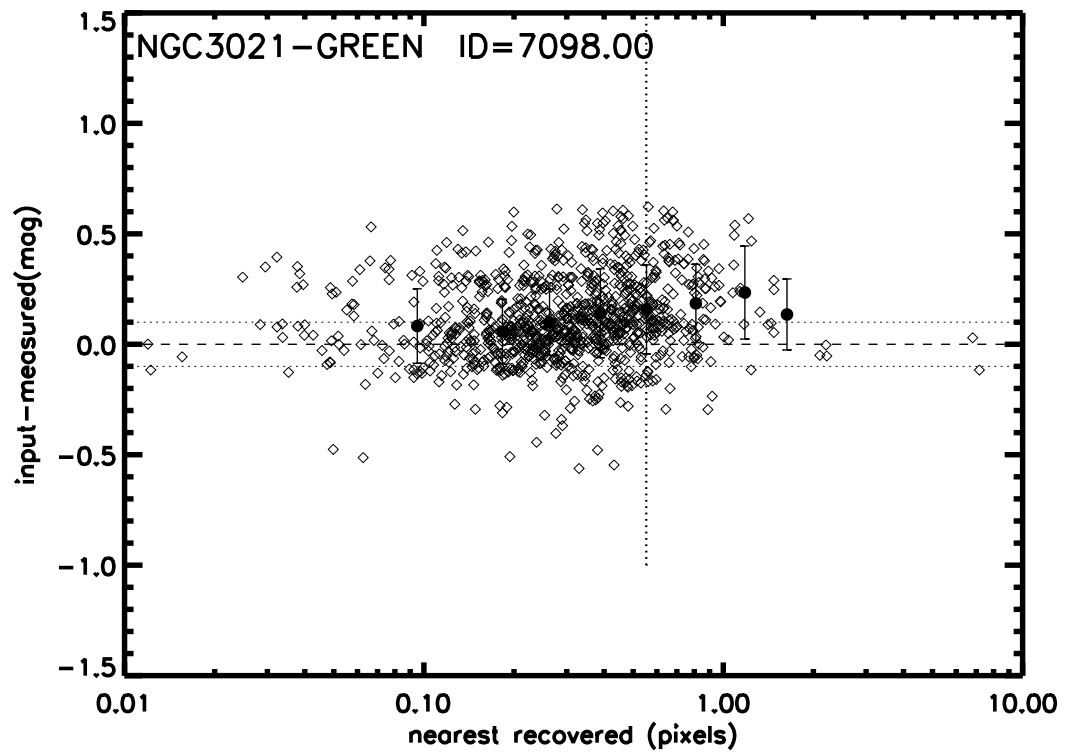


Fig. 9.—

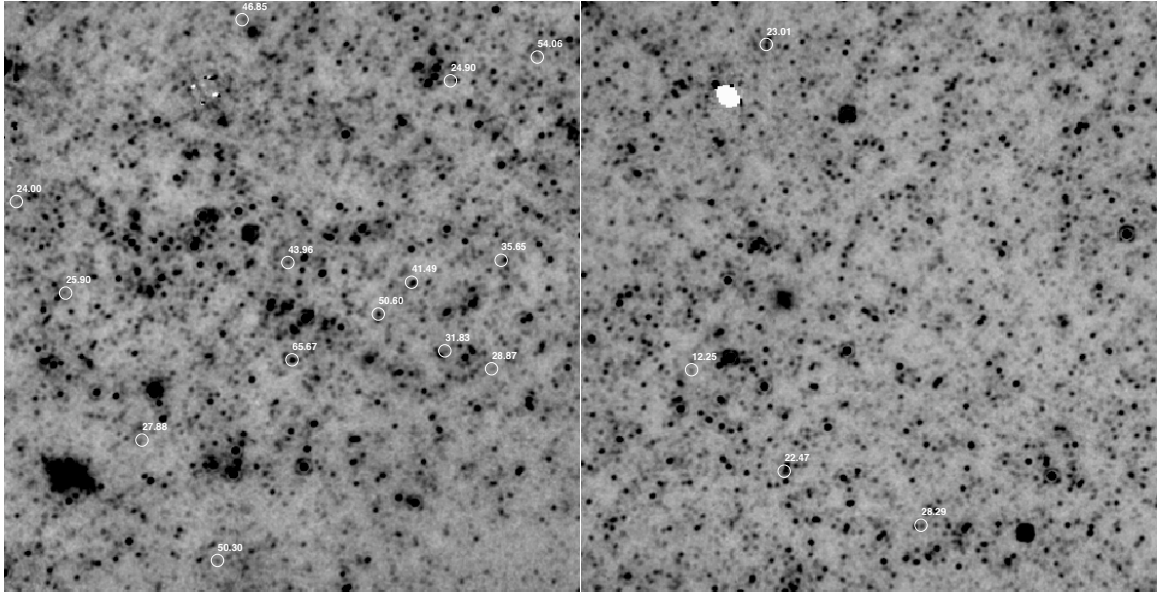


Fig. 10.—

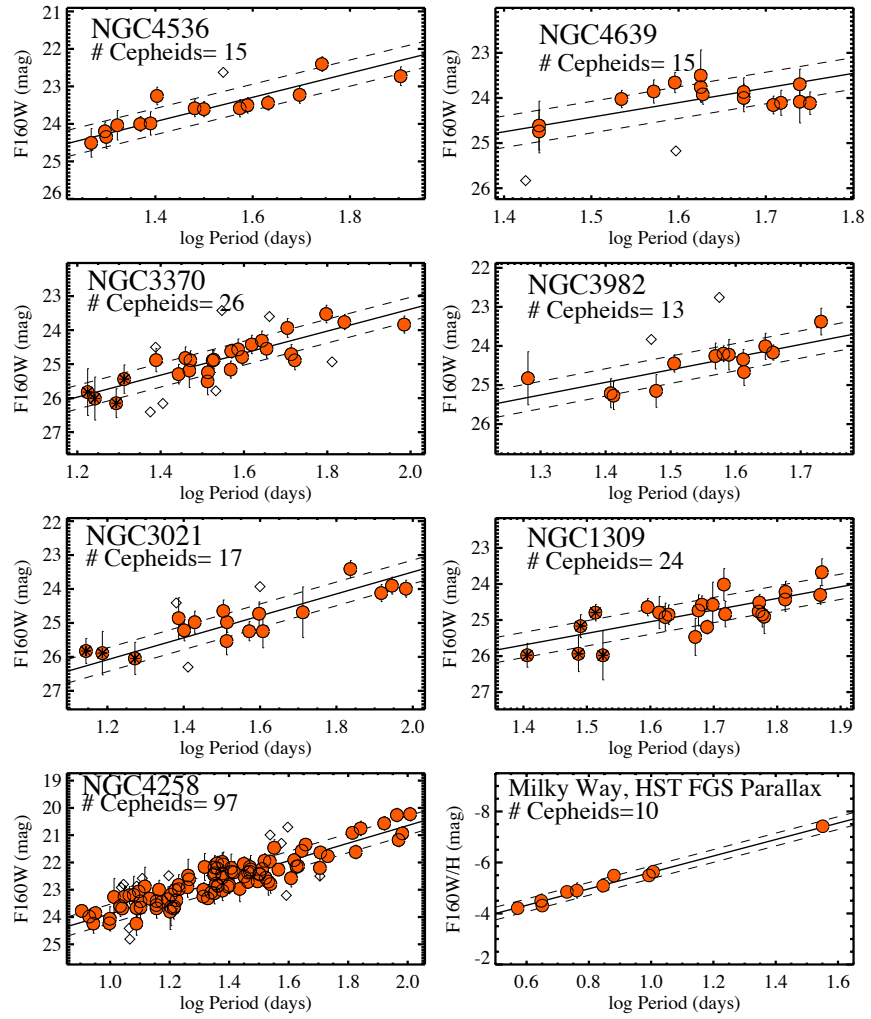


Fig. 11.—

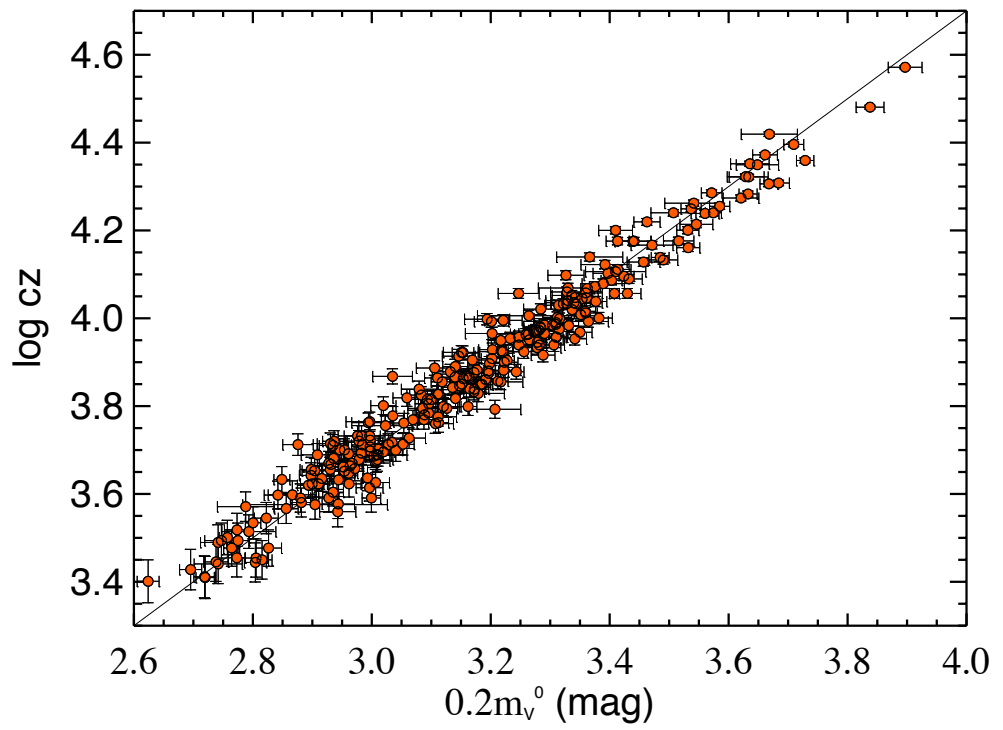


Fig. 12.—

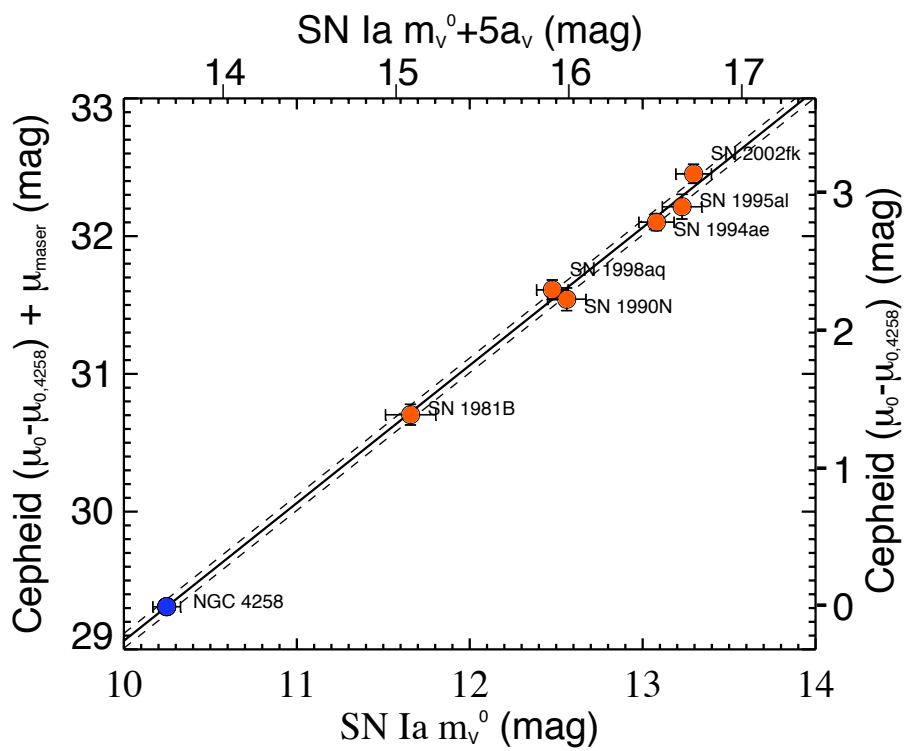


Fig. 13.—

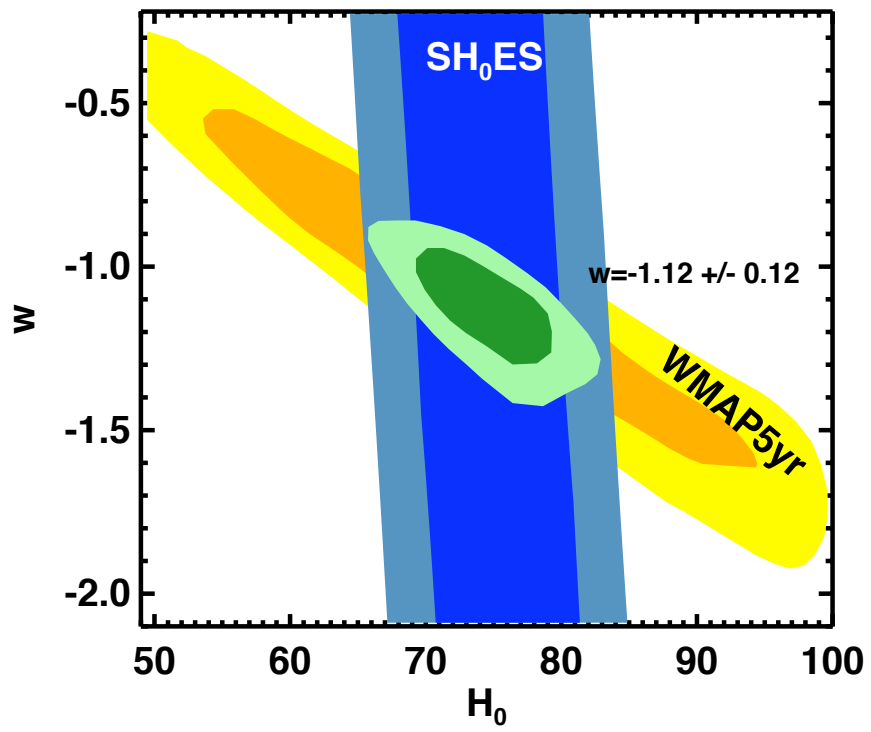


Fig. 14.—

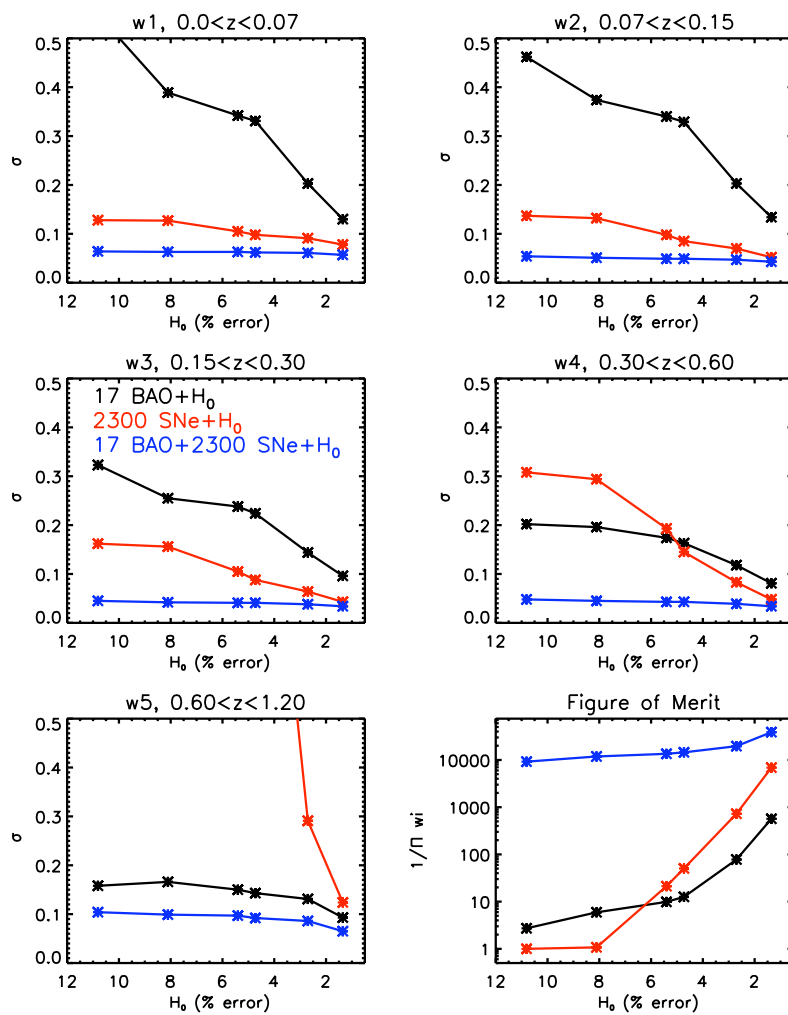


Fig. 15.—

## REFERENCES

- Astier, P., et al. 2006, *A&A*, 447, 31
- Benedict, G. F., et al. 2007, *AJ*, 133, 1810
- Berdnikov, L. N., Vozyakova, O. V., & Dambis, A. K. 1996, *Astronomy Letters*, 22, 838
- Bergeron, L. E., & Dickinson, M. E. 2003, STScI NICMOS Instrument status report 2003-010
- Bird, J. C., Stanek, K. Z., & Prieto, J. L. 2008, arXiv:0807.4933
- Braatz, J. A., Reid, M. J., Greenhill, L. J., Condon, J. J., Lo, K. Y., Henkel, C., Gugliucci, N. E., & Hao, L. 2008, *Frontiers of Astrophysics: A Celebration of NRAO's 50th Anniversary*, 395, 103
- Bushouse, H., Dickinson, M., & van der Marel, R. P. 2000, *Astronomical Data Analysis Software and Systems IX*, 216, 531
- Cardelli, J. A., Clayton, G. C., & Mathis, J. S. 1989, *ApJ*, 345, 245
- Conley, A., Carlberg, R. G., Guy, J., Howell, D. A., Jha, S., Riess, A. G., & Sullivan, M. 2007, *ApJ*, 664, L13
- Cooray, A., & Caldwell, R. R. 2006, *Phys. Rev. D*, 73, 103002
- Davis, T. M., et al. 2007, *ApJ*, 666, 716
- de Jong, R. S., Bergeron, L. E., Riess, A. G., & Bohlin, R. 2006, STScI NICMOS Instrument status report 2006-001
- Ferrarese, L., Silbermann, N. A., Mould, J. R., Stetson, P. B., Saha, A., Freedman, W. L., & Kennicutt, R. C., Jr. 2000, *PASP*, 112, 177
- Filippenko, A. V. 2005, in “White Dwarfs: Cosmological and Galactic Probes,” ed. E. M. Sion, S. Vennes, & H. L. Shipman (Dordrecht: Springer), 97
- Fouqué, P., et al. 2007, *A&A*, 476, 73
- Freedman, W. L., et al. 2001, *ApJ*, 553, 47
- Fruchter, A. S., & Hook, R. N. 2002, *PASP*, 114, 144
- Gibson, B. K., et al. 2000, *ApJ*, 529, 723
- Greenhill, L. J., Humphreys, E. M. L., Hu, W., Macri, L., Masters, K., Hagiwara, Y., Kobayashi, H., Murata, Y., 2009, *astroph0902.4255*
- Groenewegen, M. A. T. 1999, *A&AS*, 139, 245

- Guy, J., Astier, P., Nobili, S., Regnault, N., & Pain, R. 2005, *A&A*, 443, 781
- Herrnstein, J. R., et al. 1999, *Nature*, 400, 539
- Hogg, D. W., & Turner, E. L. 1998, *PASP*, 110, 727
- Hu, W. 2005, *Observing Dark Energy*, 339, 215
- Hui, L., & Greene, P. B. 2006, *Phys. Rev. D*, 73, 123526
- Humphreys, E. M. L., Reid, M. J., Greenhill, L. J., Moran, J. M., & Argon, A. L. 2008, *ApJ*, 672, 800
- Humphreys, E. M. L., Argon, A. L., Greenhill, L. J., Moran, J. M., & Reid, M. J. 2005, *Future Directions in High Resolution Astronomy*, ASP Vol 340, 466
- Humphreys, E. M. L., 2009, in prep
- Huterer, D., & Cooray, A. 2005, *Phys. Rev. D*, 71, 023506
- Huterer, D., & Starkman, G. 2003, *Physical Review Letters*, 90, 031301
- Jha, S., et al. 2006, *AJ*, 131, 527
- Jha, S., Riess, A. G., & Kirshner, R. P. 2007, *ApJ*, 659, 122
- Kim, A. G., Linder, E. V., Miquel, R., & Mostek, N. 2004, *MNRAS*, 347, 909
- Komatsu, E., et al. 2008, arXiv:0803.0547
- Leonard, D. C., Kanbur, S. M., Ngeow, C. C., & Tanvir, N. R. 2003, *ApJ*, 594, 247
- Linder, E. V., & Huterer, D. 2003, *Phys. Rev. D*, 67, 081303
- Macri, L. M., et al. 2001, *ApJ*, 549, 721
- Macri, L. M., Stanek, K. Z., Bersier, D., Greenhill, L. J., & Reid, M. J. 2006, *ApJ*, 652, 1133
- Macri, L. M., et al. 2009, *ApJ*, in press
- Madore, B. F. 1982, *ApJ*, 253, 575
- Madore, B. F., & Freedman, W. L. 1991, *PASP*, 103, 933
- Marconi, M., Musella, I., & Fiorentino, G. 2005, *ApJ*, 632, 590
- Percival, W. J., Cole, S., Eisenstein, D. J., Nichol, R. C., Peacock, J. A., Pope, A. C., & Szalay, A. S. 2007, *MNRAS*, 381, 1053
- Perlmutter, S., et al. 1999, *ApJ*, 517, 565

- Persson, S. E., Madore, B. F., Krzemiński, W., Freedman, W. L., Roth, M., & Murphy, D. C. 2004, *AJ*, 128, 2239
- Riess, A. G., & Bergeron, L. E. 2008, STScI NICMOS Instrument status report 2008-001
- Riess, A. G., Press, W. H., & Kirshner, R. P. 1996, *ApJ*, 473, 88
- Riess, A. G., et al. 1998, *AJ*, 116, 1009
- Riess, A. G., et al. 2005, *ApJ*, 627, 579
- Riess, A. G., et al. 2007, *ApJ*, 659, 98
- Riess, A. G., et al. 2009, *ApJ*, submitted
- Saha, A., Sandage, A., Labhardt, L., Tammann, G. A., Macchetto, F. D., & Panagia, N. 1996, *ApJ*, 466, 55
- Saha, A., Sandage, A., Labhardt, L., Tammann, G. A., Macchetto, F. D., & Panagia, N. 1997, *ApJ*, 486, 1
- Saha, A., Sandage, A., Tammann, G. A., Dolphin, A. E., Christensen, J., Panagia, N., & Macchetto, F. D. 2001, *ApJ*, 562, 314
- Saha, A., et al. 2006, *ApJS*, 165, 108
- Sandage, A., Tammann, G. A., Saha, A., Reindl, B., Macchetto, F. D., & Panagia, N. 2006, *ApJ*, 653, 843
- Sarkar, D., Amblard, A., Holz, D. E., & Cooray, A. 2008, *ApJ*, 678, 1
- Sarkar, D., Sullivan, S., Joudaki, S., Amblard, A., Holz, D. E., & Cooray, A. 2008, *Phys. Rev. Letters*, 100, 241302
- Sebo, K. M., et al. 2002, *ApJS*, 142, 71
- Seo, H.-J., & Eisenstein, D. J. 2003, *ApJ*, 598, 720
- Soszyński, I., Gieren, W., & Pietrzyński, G. 2005, *PASP*, 117, 823
- Spergel, D. N., et al. 2007, *ApJS*, 170, 377
- Stetson, P. B. 1994, *PASP*, 106, 250
- Stetson, P. B., & Gibson, B. K. 2001, *MNRAS*, 328, L1
- Sullivan, S., Cooray, A., & Holz, D. E. 2007, *Journal of Cosmology and Astro-Particle Physics*, 9, 4

- Tammann, G. A., Sandage, A., & Reindl, B. 2008, *ApJ*, 679, 52
- van Leeuwen, F., Feast, M. W., Whitelock, P. A., & Laney, C. D. 2007, *MNRAS*, 379, 723
- Visser, M. 2004, *Class. Quant. Grav*, 21, 2603]
- Wiltshire, D. L. 2007, *PhRvL*, 99,1101 250
- Wood-Vasey, W. M., et al. 2007, *ApJ*, 666, 694
- Zehavi, I., Riess, A. G., Kirshner, R. P., & Dekel, A. 1998, *ApJ*, 503, 483